POLYVINYL ALCOHOL AND MEDIUM DENSITY POLYETHYLENE COMPOSITE

MATERIALS FOR NEUTRON RADIATION SHIELDING

by

Glen C. King
B.S. Dec 1995, Old Dominion University
M.S. Dec 2009, Norfolk State University

A Dissertation Submitted to the Faculty of
Norfolk State University in Partial Fulfillment of the
Requirements for the Degree of

DOCTOR OF PHILOSOPHY

MATERIALS SCIENCE AND ENGINEERING

NORFOLK STATE UNIVERSITY
August, 2020

Approved by:

Kyo D. Song, Ph.D (Advisor)

Carl E. Bonner, Ph.D (Member)

Messaoud Bahoura, Ph.D (Member)

Sam-Shajing Sun, Ph.D (Member)

Sheila A. Thibeault, Ph.D (Member)

POLYVINYL ALCOHOL AND MEDIUM DENSITY POLYETHYLENE COMPOSITE

ABSTRACT

POLYVINYL ALCOHOL AND MEDIUM DENSITY POLYETHYLENE COMPOSITE MATERIALS FOR NEUTRON RADIATION SHIELDING

Glen C. King
Norfolk State University, 2020
Advisor: Dr. Kyo D. Song

Manned spacecraft venturing beyond the Earth's Van Allen Belts will be subjected to high levels of radiation from both energetic particles emanating from the sun and from galactic atomic events, such as supernovae. The metal shell of a spacecraft offers some protection from gamma radiation and high energy particles originating from both the sun and cosmic sources. The interaction of these high energy particles and radiation with the spacecraft hull create secondary radiation and neutrons, additional hazards for astronauts and electronic systems. Shielding of neutrons is the most challenging of the high energy radiation, since neutrons have zero charge and are least affected by electrical fields, magnetic fields, and atomic forces.

Previous studies showed that polyethylene is an effective neutron shielding material, due to its high hydrogen content. High energy neutrons are slowed to thermal neutrons through multiple collisions with the hydrogen atoms, increasing the effectiveness of neutron capture by boron-10 atoms. This study discusses the fabrication and testing of polyvinyl alcohol (PVOH) samples as a neutron shielding material, with comparison to medium density polyethylene (MDPE) composite samples to be used for neutron shielding for spacecraft. PVOH, an aqueous polymer, was chosen for hydrogen content and for enabling the use of organic reinforcement such as cellulose for secondary structural composites.

OLTARIS (On-Line Tool for the Assessment of Radiation in Space) was used for radiation shielding simulation and compared with experimental data. Modeling indicates that the

most effective shielding from radiation was in an aluminum layer backed by a polymer layer, either MDPE or PVOH. Cross-linked PVOH was also included in the OLTARIS modeling. All 3 polymer cases showed shielding improvement over aluminum alone, with similar dose equivalent reduction for galactic cosmic radiation (GCR) and for radiation from a solar particle event (SPE).

Fourier Transform Infrared (FTIR) Spectroscopy was used to confirm the cross-linking in the PVOH sample and to determine the uniformity through the thickness.

PVOH, cross-linked PVOH, and MDPE samples were tested for neutron shielding effectiveness using a 1 curie Americium-Beryllium neutron source. Test results indicated the most shielding in the cross-linked PVOH, followed by the pristine PVOH, and MDPE.

Neutron testing suggests that polyvinyl alcohol is a good alternative to polyethylene for neutron shielding. The neutron shielding materials, PVOH and cross-linked PVOH developed under this research will enable the safe operation of spacecraft beyond the Earth's protective Van Allen Radiation Belts. It will be crucial for NASA's manned missions to the Moon or Mars to protect the health of astronauts and equipment from the harmful effects of excessive radiation.

ACKNOWLEDGMENTS

I would like to express my sincere thanks and appreciation to my advisor, professor Kyo D. Song. His support and understanding was the best motivation I had for making progress in this research effort and was uplifting at times when I was under the most personal pressure.

I must also mention Dr. Carl Bonner's dedication to the graduate students of NSU, or more personally, to my research. His helpful discussions and suggestions helped to make my work more meaningful to the academic community.

I appreciate Dr. Sam-Shajing Sun's persistence in improving my understanding of polymers. Much of what I know about polymers was what I learned in his classes. His class on the photovoltaic applications made me more alert to the optical applications of polymers.

I thank Dr. Messaoud Bahoura for his selfless support and encouragement, and sincere engagement in ensuring the success of my research.

I appreciate Dr. Govindarajan Ramesh for his interest, contributions to, and realization of the importance of space radiation on the health of astronauts and his efforts to keep me engaged in this important work.

Dr. Sheila Thibeault has always been a big supporter for my radiation materials development and testing. She always made sure to include my name in the colloquiums and business presentations related to radiation shielding, radiation modeling, and health effects of radiation exposure.

I would like to thank Dr. Sang-Hyon Chu for taking the time to show me the nuances of our infrared spectrometer and how to get meaningful results.

I also appreciate the time that Eric Hoffman gave to help with the tables, figures and captions not updating properly.

I would also like to express my appreciation for my wife Ann (Cheyenne) for tolerating my absence while taking classes, the often lack of free time, and for her understanding of my determination for completing this research. I am thankful for the many times she individually took care of the responsibilities and unforeseen events encountered in raising our son.

Glen C. King
Norfolk State University
2020

TABLE OF CONTENTS

LIST OF TABLES

LIST OF FIGURES

LIST OF ACRONYMS

ACE	Advanced Composition Explorer
BNNT	Boron Nitride Nanotubes
CME	Coronal Mass Ejection
CREAM	Cosmic Radiation Effects and Activation Monitor
FTIR	Fourier Transform Infrared
GCR	Galactic Cosmic Radiation
HZE	High Atomic Number and Energy
HZETRN	High Charge and Energy Transport
ICRP	International Commission on Radiological Protection
IR	Infrared
LEO	Low Earth Orbit
MCNP	Monte Carlo N–Particle Transport Code
MDPE	Medium Density Polyethylene
MISSE	Materials International Space Station Experiment
NASA	National Aeronautics and Space Administration
NCRP	National Council on Radiation Protection & Measurements
NRC	Nuclear Regulatory Commission
OLTARIS	On- Line Tool for the Assessment of Radiation in Space
PE	Polyethylene
PHITS	Particle and Heavy Ion Transport code System
PVOH	Polyvinyl Alcohol
SAM	Shuttle Activation Monitor

SEP	Solar Energetic Particle
SPE	Solar Particle Event

21. INTRODUCTION

1.1 Research Description and Motivation

NASA is currently implementing plans to return to the Moon and land humans on the surface by 2024. There will be a permanent human presence, and it will also be used as a starting point for a planned Mars mission [1]. In addition to expanding human presence beyond Earth, the effort will establish a lunar-based economy for the benefit of US companies and international partners. As a result, not only will the astronauts and electronic equipment need protection from high energy protons and ions during the trip, but any habitat or lunar/Martian excursions will require some reliable form of radiation shielding. The interaction of protons and ions with the metal hull of spacecraft or other metallic structures produces secondary neutron radiation. The development of effective neutron radiation shielding was therefore the motivation for this research.

The main purpose of this research was to develop and characterize polyvinyl alcohol (PVOH) samples, both pristine and cross-linked, to be used for neutron radiation shielding applications. The use of borax was intended to increase the hydrogen content, the boron content, and to crosslink the PVOH chains. Samples of medium density polyethylene (MDPE) were also fabricated and tested to be used as a baseline and to test the effectiveness of neutron moderation and capture. Four weight percent concentrations of boron nitride nanotubes (BNNTs) in an MDPE material were also developed to determine suitability as a spacecraft radiation shielding material and to determine the effect of boron distribution in a stacked configuration, with varying BNNT concentration in each layer. The BNNTs add structural functionality and boron to the MDPE. Previous research at NASA Langley Research Center indicated that materials with high hydrogen content such as polyethylene are the most effective for reducing high energy neutrons

to thermal energy levels [2, 3, 4]. One such study discusses multifunctional radiation shielding materials involving polyethylene and hydrogenated nanotubes as an enhancement to shielding materials for spacecraft [5]. The BNNTs were selected for their structural properties and for adding boron to the composite. Boron isotopes occur naturally as 20% boron-10 and 80% boron-11. It is well established that for neutrons at thermal energy levels, boron-10 is the most effective and economical isotope for capturing neutrons. The previous studies at NASA Langley Research Center were also a motivating factor for this research.

1.2 Significance of Research

Research in radiation shielding materials will produce radiation protection technology enabling future space exploration missions. In general, the level of exposure to ionizing radiation is determined by: 1) exposure time, 2) distance from the radiation source, and 3) shielding. The first two factors will be determined by the nature of the mission. The distance factor for a radiation point source follows the inverse square law, Eq. 1. [6]:

$$I \propto \left(\frac{1}{d}\right)^2 \tag{1}$$

where I = the intensity (dose, or dose rate) and d = distance from the radiation source. For comparison of two distances, a ratio can be applied as in Eq. 2:

$$I_2 \propto I_1 \left(\frac{d_1}{d_2}\right)^2 \tag{2}$$

For example, the intensity I_2 will be reduced to ¼ that of I_1 if the distance from the radiation source, d_1, is doubled (d_2). However, this relation applies to radiation from a point source only that is not distorted by a magnetic field. Although Solar Particle Events (SPEs) appear to be applicable, the Sun's and the Earth's magnetic fields can distort the radiation from the Sun, and the intensity will vary according to the solar cycle. In the case of GCR, there is no

safe distance, since it radiates from every direction, so historical measurements are required for modeling incident radiation.

Sunspot activity follows a cycle of 11 years, alternating between the solar maximum (the most sunspot activity) and the solar minimum [7]. During the solar maximum, the Sun's magnetic field is extended, reducing the effective dose of SPE and GCR radiation. During a solar maximum, for example, GCR is reduced to about half that of a solar minimum. Shielding will be the one factor that can limit the radiation exposure to astronauts both during travel beyond the Earth's magnetic field and for lunar, Martian, or near-Earth planetary based habitats. It will likely be a determining factor to enable long-duration missions beyond planet Earth.

This research addresses the shielding requirement with a lightweight, inexpensive radiation shielding material that will be suitable for spacecraft and missions beyond the Earth's ionosphere. Material durability of samples developed in this research will eventually be investigated after exposure in a space environment (LEO) on the International Space Station as part of the Materials International Space Station Experiment (MISSE). It is likely that PVOH shielding materials will have many terrestrial applications as well, such as in the medical field, the military, neutron generating research facilities, and the nuclear power industry.

1.3 The Radiation Environment

A few years after confirming the existence of the Van Allen radiation belts in 1958, scientists working on the Apollo lunar missions knew that space radiation and charged particles would be a major consideration in sending the Apollo astronauts to the Moon. To alleviate these hazards, a radiation protection plan was developed based on real-time monitoring of solar activity and radiation in the spacecraft in addition to worldwide solar activity monitoring to predict upcoming radiation hazards, such as solar flare particle events [8]. Additionally, lunar

excursions were preceded by low altitude earth orbits and rapid transits through the Van Allen belt to keep the astronaut radiation dose below 1 rad [9]. Astronauts will again face these hazards in addition to solar particle events (SPEs), occasional coronal mass ejections (CMEs), and long term exposure from galactic cosmic rays (GCR) when traveling to and living on the Moon or Mars. The same can be said of any long-duration space travel or manned presence beyond the protection of Earth's protective magnetic field.

Space radiation (SPEs, CMEs, and GCR) consists of gamma rays, high-energy protons, electrons, and HZE (high atomic number and energy) ions and can have energies in the GeV range. Both SPEs and CMEs from the Sun are influenced by the solar maximum and solar minimum of the eleven-year solar cycle. The solar maximum is the part of the solar cycle in which the maximum number of sunspots appear and solar irradiance grows by about 0.07% [10]. About 2 or 3 SPEs per day occur during the solar maximum, compared to 1 SPE during solar minimum [11]. Ironically, the increased solar activity at solar maximum extends the solar magnetic field, resulting in lower radiation levels for the inner solar system. For example, astronauts aboard the International Space Station receive an average of 80 mSv for a six-month stay during solar maximum, but an average of 160 mSv for a six-month stay during solar minimum [12].

The inevitable exposure to cosmic radiation that is expected to cause serious health problems will require radiation shielding materials to protect the astronauts, especially for particles and electromagnetic energy that are not shielded by the hull of the spacecraft. High energy protons and HZE ions cause secondary radiation and can generate neutrons when they collide with atoms in the spacecraft hull. It has been proposed that space shuttle flight samples monitored with the Shuttle Activation Monitor (SAM) and the Cosmic Radiation Effects and

Activation Monitor (CREAM) indicate a factor of 2 difference in the radiation spectrum with secondary radiation considered and with it omitted [13].

Several studies, both computational and experimental, are published quantifying the extent and studying the effects of radiation in space. Radiation transport codes, such as HZETRN (High Charge and Energy Transport), OLTARIS (On-Line Tool for the Assessment of Radiation in Space, uses HZTERN), PHITS (Particle and Heavy Ion Transport code System), MCNP (Monte Carlo N–Particle Transport Code), and several others are used to determine the radiation transport through materials.

There are several publications on the radiation exposure expected and measured, both in transit and on the surface of Mars [14, 15]. The Martian rover Curiosity took measurements of the radiation both in-transit and on the surface of Mars using the Radiation Assessment Detector (RAD). This instrument characterized the full spectrum of energetic particle radiation at the surface of Mars, including GCRs, solar energetic particles (SEPs), secondary neutrons, and other particles created both in the atmosphere and in the Martian regolith. [16].

1.4 Health Hazards From Radiation

High energy particle radiation in a space environment creates neutrons and secondary radiation from atomic collisions within the hull of a spacecraft or from collisions with the lunar or Martian surface. Reducing the energy of neutrons and capturing them can minimize human biological damage resulting from secondary neutron radiation. It is therefore important to also realize the harm that neutrons pose in addition to other particles and electromagnetic radiation from GCR and SPEs. Absorbed dose, dose equivalent, and the effective dose are used as measures of radiation effects for different conditions (see Fig. 1). Absorbed dose, D, is the amount of energy deposited in a material by radiation. Doses are all measured in

Joules/kilogram, with the absorbed dose given in Greys (Gy) and both equivalent dose and effective dose given in Sieverts (Sv). For each type of radiation, the equivalent dose is determined by multiplying the absorbed dose by a radiation weighting factor, w_R. For situations where only certain areas of the body absorb the radiation, the equivalent dose is multiplied by a tissue weighting factor to give the effective dose. For space radiation, the entire body is usually affected, so the magnitude of the effective dose equals that of the equivalent dose.

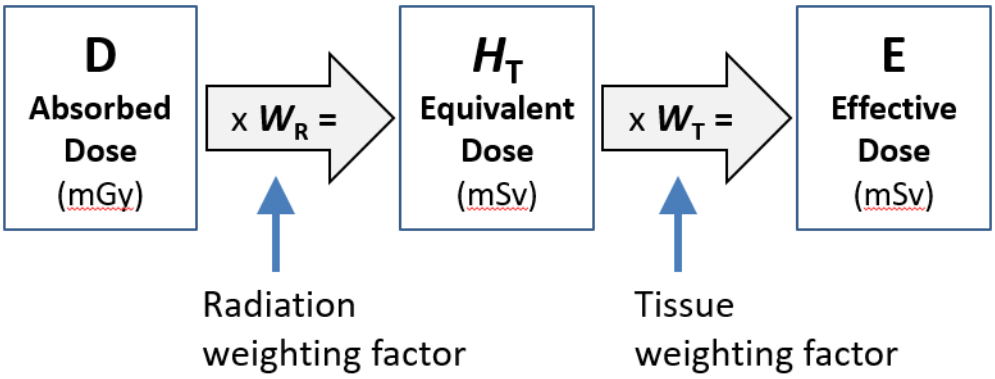

Fig. 1: Absorbed Dose, Equivalent Dose, and Effective Dose Relationship.

The 2007 recommendations of the International Commission on Radiological Protection (ICRP), Table A-2, [17] lists the radiation weighting factors for each type of radiation, as shown in Fig. 2.

Radiation type	Radiation weighting factor, W_R
Photons	1
Electrons and muons	1
Protons, and charged pions	2
Alpha particles, fission fragments, heavy ions	20
Neutrons	$w_R =$

ref. 2007 Recommendations of the ICRP

$$w_R = \begin{cases} 2.5 + 18.2e^{-[\ln(E_n)]^2/6}, & E_n < 1 \text{ MeV} \\ 5.0 + 17.0e^{-[\ln(2E_n)]^2/6}, & 1 \text{ MeV} \le E_n \le 50 \text{ MeV} \\ 2.5 + 3.25e^{-[\ln(0.04E_n)]^2/6}, & E_n > 50 \text{ MeV} \end{cases}$$

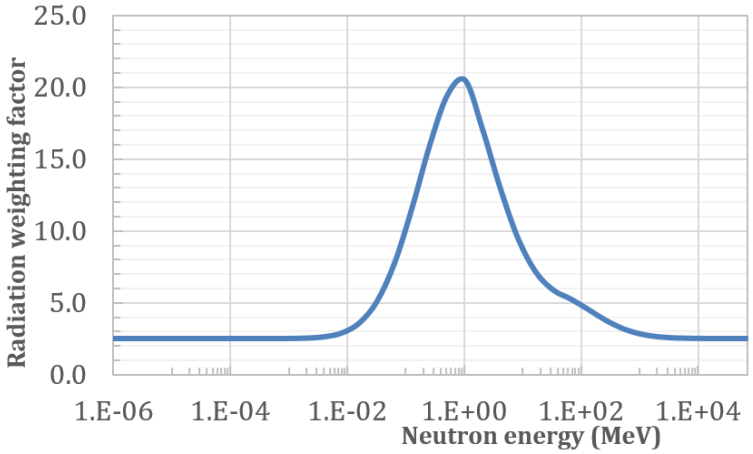

Fig. 2: ICRP recommended radiation weighting factors.

Since SPEs and GCR are each composed of different types of radiation, different radiation weighting factors are considered in determining the equivalent dose, H_T, according to Eq. 3:

$$H_T = \sum_R w_R D_{T,R} \quad (3)$$

where w_R is the radiation weighting factor and $D_{T,R}$ is the average absorbed dose from radiation R in a tissue or organ T. Note that the neutron radiation weighting factor is dependent on the neutron energy, and is between 2.5 and about 20. The importance of shielding can be seen by comparing SPE and GCR radiation consisting mostly of protons ($W_R = 2$), electrons ($W_R = 1$), and heavy ions ($W_R = 20$) to that of secondary radiation consisting of an abundance of neutrons. The ICRP recommended tissue weighting factors listed in Table 1 add up to 1.00, so the equivalent dose is used in this research.

Table 1. ICRP Tissue Weighting Factors.

Tissue or organ	Tissue weighting factor, w_T	Σw_T
Bone-marrow (red), Colon, Lung, Stomach, Breast, Remainder tissues	0.12	0.72
Gonads	0.08	0.08
Bladder, Oesophagus, Liver, Thyroid	0.04	0.16
Bone surface, Brain, Salivary glands, Skin	0.01	0.04
	TOTAL	**1.00**

ref. 2007 Recommendations of the ICRP

For situations that result in partial shielding of the body (i.e. shielding vests or helmets), the ICRP recommends a similar calculation for determining the effective dose, E (Eq. 4):

$$E = \sum_T w_T H_T = \sum_T w_T \sum_R w_R D_{T,R} \quad (4)$$

where w_T is the tissue weighting factor, H_T is the equivalent dose of incident radiation, w_R is the radiation weighting factor, and $D_{T,R}$ is the absorbed dose from radiation R in a tissue or organ T.

The Nuclear Regulatory Commission established the yearly radiation dose limits for radiation workers (on Earth), as shown in Table 2. The limits are weighted for different parts of the human body. The dose limits are the same as those established by the National Council on Radiation Protection & Measurements (NCRP) [18] and the NASA-STD-3001: NASA space flight human system standard, volume 1 lists the permissible exposure limits (PELs) and radiation health for several environmental conditions [19]. The standard follows the NCRP

Table 2. Yearly Occupational Dose Limits

U.S. NRC Yearly Occupational Dose Limits		
	Millirems (mrem)	Millisieverts (mSv)
Whole Body	5,000	50
Any Organ	50,000	500
Skin	50,000	500
Extremity	50,000	500
Lens of Eye	15,000	150

recommendations for exploration class missions. NASA's planned career radiation exposure rates vary with astronaut age and gender, but are not to exceed 3 percent risk of exposure-induced death (REID) for fatal cancer.

It is important to realize that even though the effects of radiation exposure in a short period, such as during a solar particle event, may be within the yearly dose limit, it still may be extremely damaging. For any SPE, immediate protection could be essential. There are currently several publications that attempt to quantify the damaging effects of radiation on astronauts in a space environment [20]. John Charles, a cardiovascular physiologist and chief scientist for NASA's Human Research Program, listed as one of the top concerns for the agency's human deep space ambitions: Exposure to cancer-inducing solar and cosmic radiation from which humans are normally shielded by the Earth's magnetic field [21]. The National Space Biomedical Research Institute (NSBRI), a NASA-funded consortium of institutions, has published numerous papers that identify the risks of space radiation, the effects, and mitigation of the effects through techniques in genomics, proteomics, metabolomics, and other biological techniques [22].

For both lunar and Mars missions, both acute and chronic radiation effects have been the subject of much research. Acute effects are usually the result of high exposures to radiation, with symptoms such as burns, radiation sickness (nausea, vomiting, diarrhea, bleeding, hair loss, weakness, and organ damage), or death. SPE radiation is a major concern for causing acute radiation illnesses. Chronic effects of radiation are the result of long-term exposure to lower levels of radiation, such as GCR. They include DNA mutations and cancer. Researchers have studied, in particular, the radiation effects on the brain cognition, the central nervous system, the heart, and vision.

Vascular damage in the brain has been observed in previous experiments involving boron neutron capture therapy. Radiation injury to the central nervous system as a result of the blood-brain barrier damage can lead to cell death, gene expression changes, and a toxic microenvironment [23]. The blood-brain barrier is a thin layer of protective cells that restrict the passage of pathogens and solutes in the blood from entering the central nervous system, while selectively allowing nutrients, glucose and other essentials for neural function to pass through.

Long-term lower-levels of radiation have also been shown in mouse models to cause serious mental degradation. A recent study shows that rodents exposed to cosmic radiation exhibit persistent hippocampal and cortical based performance decrements using six independent behavioral tasks administered between separate cohorts 12 and 24 weeks after irradiation [24]. Another study exposed 40 mice to a low radiation dose rate of 1 mGy/d for 6 months. Severe learning and memory impairments were then observed, with the emergence of distress behaviors [25]. Although the rodent models for radiation damage assessment can identify health concerns, it should also be noted from research by F.A.Cucinotta et al (refer to Table 2) that the rodent models have many limitations when comparing to humans [26].

Cardiovascular effects from space radiation may be harder to discern due to the absence of Earth's gravity or the frequency of exercise, both beneficial to cardiovascular health. Although the sample population was quite small, the effects of space radiation have indicated a higher incidence of heart conditions among the Apollo astronauts, about 4-5 times higher than in astronauts exposed to space radiation in low Earth orbit. The research conducted by Florida State was the first comparison of Apollo astronauts to other astronauts. However, the small number (24) of Apollo lunar astronauts and the lack of lifestyle factor considerations such as genetics and diet may have skewed the results [27, 28]. Because of the small sample population, it may be more reasonable to look at other cases for cardiovascular effects, especially for long-term exposure. Chronic, low-level radiation exposure is a risk factor for atherosclerosis and increases the risk of cardiovascular disease, an indication reported by radiation-therapy patients, atomic bomb survivors, and radiation technicians [29, 30].

Space radiation is also suspected of affecting vision, according to a 2004 astronaut survey by questionnaire. Among the 59 European Space Agency and NASA astronaut respondents, 47 reported seeing flashes of light with no visible cause [31, 32]. Apollo astronauts Edwin Aldrin and Charles Conrad reported that flashes or streaks of white light were seen with a frequency of 2 per minute [33]. The same article also reports that human research at the Berkeley 184-inch (467-cm) cyclotron suggests that the flashes are most likely due to proton recoils induced by the fast neutron atomic collision near the retina. Two NASA space shuttle experiments (on STS-133 and STS-135) with mice were the first to see the loss of gene expression that aids in cells functioning with retinal oxidative stress [34, 35]. Although this damage was partially reversible, other permanent cellular-level damage was noted in the optic nerve.

The growing concern over the health of astronauts venturing beyond Earth's magnetosphere is reflected in the numerous ongoing research studies on radiation shielding as well as the NASA-supported small business research solicitations [36] in radiation protection materials development. For long-duration space travel or long term residence on the lunar or planetary surfaces, protection from GCR and SPEs is imperative.

1.5 State-of-the-Art Radiation Shielding Methods

1.5.1 Active shielding systems. There are three main types of active radiation shielding systems in development today. The proposed systems either trap or deflect charged particles using a magnetic field, an electrostatic field, or a plasma shield. Incident GCR and SPE radiation lack neutrons since the half-life of isolated neutrons is about 14 minutes and 39 seconds. Active radiation shielding systems are designed to shield the spacecraft from GCR and SPE radiation to prevent or minimize secondary radiation (and neutrons) generated within the spacecraft hull.

Magnetic Shielding consists of a system to generate a magnetic field around the spacecraft using electromagnetic components or superconducting coils to deflect charged particle radiation. Effective shielding from high energy charged particles for both an electromagnetic system and a superconducting coil system requires field strengths that imply a prohibitively large shielding mass for spacecraft [37].

Electrostatic Shielding is a system creating an outwardly facing electrical field surrounding the spacecraft to slow or deflect charged particle radiation. The charge arrangement can vary widely and might consist of solid or meshed toroidal or spherical components surrounding the spacecraft [38]. The arrangement often consists of an inner positively charged

electrical field and an outer negatively charged field, similar to the Earth's Van Allen radiation belts.

Plasma shielding uses a plasma of negatively charged particles confined by a magnetic field. As protons and positively charged particles approach a spacecraft, the plasma particles, being oppositely charged, are propelled to enormous speeds and intercept the incoming (mostly proton) flux. One advantage of plasma shielding is that the magnetic field required to confine the electron plasma is much weaker and requires less energy than that required to redirect protons, as in the magnetic shielding system. It is suggested that this will lead to bigger weight savings as well [39].

A review of the proposed active methods require unique considerations in addition to achieving efficient shielding. Health effects from strong electrical or magnetic fields require consideration. Previous research on the health effects of static magnetic fields in general often led to inconclusive results [40]. However, a few studies have shown evidence that exposure to electromagnetic fields at non-thermal levels can disrupt the blood-brain barrier surrounding the brain [41]. The potential health hazards from active shielding systems will require modeling and monitoring for acceptable field strength within the spacecraft. Magnetic or electrostatic systems could also affect the electronics and communications as well. The system weight, power requirements, and reliability will also be a major concern, regardless of the active system employed. Trapped or deflected ions may also produce secondary neutron radiation through collision with incident GCR and SPE protons and ions.

1.5.2 Passive shielding systems. Passive shielding systems are made of materials that reduce or eliminate radiation propagation without the need for power generation systems, cooling systems, or system maintenance. Shielding for gamma or x-rays are most effective when

heavier elements are used. Previous researchers have investigated PVOH composites for gamma or x-ray shielding that use lead atoms in lead nitrate paint [], iron atoms in the form magnetite [,], tungsten atoms in tungsten oxide (WO_3) [], titanium atoms in titanium dioxide [], barium atoms in barium sulfate [], etc. Although these are good for shielding photon radiation, they can also produce more penetrating particle radiation (neutrons) when used as shielding from gamma or high energy ions []. For shielding in a space radiation environment, passive radiation shielding is most effective using the metal spacecraft hull with an internal polymer layer to attenuate secondary radiation.

For spacecraft shielding materials to be flown on spacecraft, the material weight becomes a critical factor to be considered. Unlike for spacecraft applications, terrestrial applications of radiation shielding materials often have few weight and dimensional constraints. For example, nuclear reactors, accelerators, and high energy research facilities can use cement, lead, and water for shielding materials. The same materials would not be practical for spacecraft. Spacecraft shielding materials for astronaut missions are required to possess properties that are often more stringent than Earth-based applications. An effective shielding composite for spacecraft will entail the following considerations:

1. Light weight, to reduce launch cost.
2. Low material cost and fabrication cost making it economically feasible.
3. Non-toxic outgassing to be suitable for the closed and isolated environment of a spacecraft.
4. Secondary structural application (multifunctional) is desired to preclude parasitic weight.

5. Effective reduction of the radiation dose rate for astronauts in a space radiation environment.

There are two mechanisms for minimizing neutron radiation propagation through a material: neutron moderation (elastic or inelastic/non-elastic collision with atoms) and neutron absorption or capture (Fig. 3). Hydrogen and hydrogen-containing materials (cement, concrete, polymers, water, etc.) have been shown to reduce the energy of neutrons to enable neutron capture, such as with boron-10 [49]. Since hydrogen has the least mass of all elements, it can remove more kinetic energy from neutrons. Inelastic collision of the neutron with the hydrogen atom transforms some of the kinetic energy of the fast neutron to potential energy in the hydrogen atom, potentially reducing fast (> 10 KeV) neutrons to thermal (< 1 eV) neutrons. Additional collisions of the neutron with other hydrogen atoms will eventually become predominantly elastic (a scattering event), conserving both total kinetic energy and momentum in the collision. As Fig. 3 shows, the polyethylene or PVOH functions as the moderator, while the boron-10, after absorbing a neutron, becomes an excited Boron-11 atom that undergoes instantaneous fission, releasing gamma energy, an alpha particle (Helium-4), and a Lithium-7 nucleus.

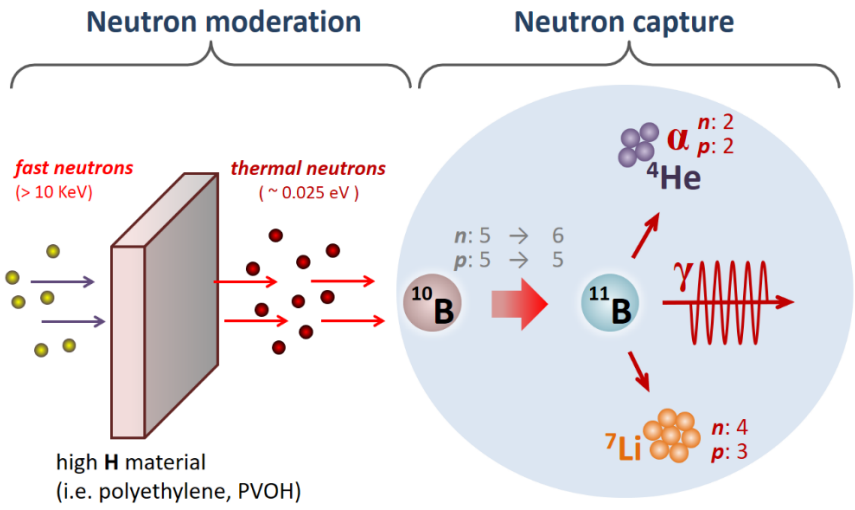

Fig. 3: Moderation and capture mechanisms for neutron shielding.

Most naturally occurring isotopes and elements (having multiple isotopes) in the periodic table have been characterized for neutron scatter and absorption and have a radiation cross-section, expressed in barns (10^{-24} cm^2), associated with it. Table 3 is an abbreviated list of scattering and absorbing cross-sections, originally compiled by Alan Munter of the NIST Center for Neutron Research [50] using data from V.F. Sears, published in Neutron News [51]. The barn is an approximation of the cross-sectional area of a uranium nucleus, although the radiation cross-section is a measure of the probability of neutron capture and not a physical dimension.

Table 3. Selected, Largest Neutron Radiation Cross Sections for Scattering and Absorption.

Neutron Radiation Cross Sections			
		Cross Sections	
Isotope	Percent Concentration	Scattering (Barns)	Absorption (Barns)
Dy	all isotopes	90.3	994.(13.)
^{143}Nd	12.18	80.(2.)	337.(10.)
^{36}Ar	0.337	77.9	5.2
^{102}Ru	31.6	144.8	1.17
^{1}H	99.985	82.03	0.3326
H	all isotopes	82.02	0.3326
^{157}Gd	15.7	1044.(8.)	259000.(700.)
^{164}Dy	28.1	307.(3.)	2840.(40.)
^{196}Hg	0.2	115.(8.)	3080.(180.)
^{149}Sm	13.9	200.(5.)	42080.(400.)
Gd	(all)	180.(2.)	49700.(125.)
^{151}Eu	47.8	8.6	9100.(100.)
^{155}Gd	14.8	66.(6.)	61100.(400.)
Sm	all isotopes	39.(3.)	5922.(56.)
^{3}He	0.00014	6	5333.(7.)
Eu	all isotopes	9.2	4530.(40.)
^{10}B	20	3.1	3835.(9.)
^{184}Os	0.02	13.(5.)	3000.(150.)
Cd	all isotopes	6.5	2520.(50.)
^{168}Yb	0.14	2.13	2230.(40.)
^{199}Hg	17	66.(2.)	2150.(48.)
^{176}Lu	2.61	5.9	2065.(35.)
^{113}Cd	12.22	12.4	20600.(400.)

Notes: Only **Scattering** > 70 Barns are highlighted
Only **Absorption** > 1900 Barns are highlighted
Cross sections in parenthesis are uncertainties.
absorption cross section for 2200 m/s neutrons (thermal)

The scattering and absorption cross-sections are applicable for thermal neutrons with a kinetic energy of 0.025 eV and a speed of 2,200 m/s ($k = ½ m v^2$). Only the isotopes with a scattering neutron radiation cross-section greater than 70 barns and those with an absorption cross-section greater than 1,900 barns were considered. 70 barns was selected to limit the isotopes to those having the best scattering ability. The selections for both scattering and absorption are in the

dark bordered, highlighted cells in Table 3. It can be seen that hydrogen, with 82 barns, is the best option for scattering since it is the most abundant of the isotopes and is available in water and numerous hydrocarbons. It is also the reason why polyethylene and polyvinyl alcohol are excellent moderators. The 1,900 barns limit for the absorption cross-section was chosen as half that of boron-10, and to limit the list to the most promising materials to be considered for neutron capture. A more recent study found that that Zr-88 has a thermal neutron capture cross-section of 861,000 ± 69,000 barns, the second-largest thermal neutron capture cross-section known [52]. However, it is radioactive and therefore not suitable use in manned structures. Of those selected from the list, boron-10 is a good choice because it is not radioactive, is non-toxic, and is easily available in many forms (i.e. boron nitride and boron hydrates). Most importantly, at neutron thermal energy, Boron-10 has the highest neutron radiation cross-section (>3800 Barns) of all common isotopes.

1.6 Selection of Materials

There are several considerations in materials selection that can enhance the neutron radiation shielding ability. Fortunately, for spacecraft applications materials consisting of lighter atoms have a few advantages over metals. Polyethylene and polyvinyl alcohol were chosen for this research because of their high hydrogen content and very large molecular composition. Hydrogen atoms do not have neutrons, therefore, they are closest in size to the secondary neutrons. This condition makes hydrogen atoms extremely efficient in reducing the kinetic energy of fast neutrons to thermal/potential energy. The large molecules increase the number of collisions through the thickness of the polymer layer. Polymer composites are also well known for reducing the secondary radiations (γ rays, protons, and alpha particles) from neutron-atomic

interactions [53]. In the case of PVOH shielding materials, both its carbon and oxygen nuclei tend to disintegrate into helium nuclei under GCR irradiation without producing neutrons [54].

Previous research at NASA Langley Research Center identified a combination of polyethylene with fillers or reinforcing materials containing boron-10 as having the most effective neutron shielding ability [55]. A study published in 1998 showed that a 0.5 cm thick sample of the polymer K3B containing 15% amorphous boron powder absorbed over 90% of incident thermal neutrons [56].

Several other materials were considered by researchers to include both the scattering and capture mechanisms for neutron shielding. One often-considered element is lithium. Lithium, in its natural isotope distribution, has a neutron cross-section of 70.5 barns, while boron's is 767 barns (both from the Sears reference table) [57]. One study used a lithium hydride and boron mixture to eliminate the (organic) polymer component, raise the operating temperature, and to lower the level of gamma (0.42 MeV) radiation emitted from boron-10 after neutron capture [58]. Zirconium borohydride and zirconium hydride were also found effective for high-temperature applications where the neutron energy was below 100 eV [59]. Okuno found that a Colemanite-filled epoxy had about 3 times the strength of concrete and suitable performance as a neutron shield for up to 133°C [60]. The Colemanite, a hydrous calcium borate mineral, functions as a filler rather than a reinforcement. Researchers have also studied a flexible thermal neutron radiation shielding using natural rubber and natural rubber/wood composites with boron oxide (B_2O_3) or boric acid (H_3BO_3) [61]. A common goal for these and several other researchers is to increase the operating temperature of the neutron shielding system [62, 63, 64, 65]. Although neutron shielding materials with a high operating temperature are necessary for some applications, the MDPE and PVOH composites for this research were selected for applications

within the living and working space of manned spacecraft. Both MDPE and PVOH composites would be multifunctional (structural and neutron shielding) to eliminate parasitic weight. Therefore, the materials were selected for optimizing the neutron radiation shielding performance using both the scattering and absorption functionalities; MDPE with BNNT reinforcement and PVOH with borax as a cross-linker for enhanced neutron shielding ability.

The effectiveness of Boron-10 in capturing low energy neutrons ranging from 10^{-5} to 10^{4} eV and the effect of hydrogenation for slowing down high energy neutrons is the focus of many research efforts [66, 67, 68]. One study using Colemanite, a secondary mineral of borax, in an epoxy matrix showed a better neutron dose attenuation than a polyethylene/10% boron oxide composite, although it is unknown to make a suitable structural component for spacecraft [69]. Although naturally occurring forms of boron such as borax are 20% boron-10 and 80% boron-11 isotope content, enriched products are commercially available [70, 71, 72, 73]. The natural distribution was used in this research to allow comparison with previous shielding materials research.

Polyethylene (or other polymers) with boron nitride nanotubes is a well-studied shielding composite and makes a good baseline material for comparing to PVOH and cross-linked PVOH.

Polyvinyl Alcohol is a water-soluble, synthetic chain polymer with the chemical formula $CH_2CH(OH)]_n$. It was chosen for the matrix material due to its ability to form long chains, each with a hydroxyl group (OH) and its ability to be cross-linked with borax (the boron component). The OH also has a slight negative charge that easily forms a hydrogen bond with the slightly positive water molecule. This makes cellulose a compatible reinforcement for PVOH materials. Processed cotton fiber, for example, is about 99% cellulose. Cellulose is composed of long chains of glucose molecules, each with three hydroxyl groups (OH). Since the glucose chains

are extremely long in cotton fiber, it functions as a method of increasing hydrogen in the composite material. Cellulose can absorb water, oil, and other liquids, binding 4-9 times its own weight in water [74]. Since much research on PVOH/cellulose composites currently exists [75, 76, 77], the focus will be on the neutron radiation shielding ability of the matrix materials, PVOH and cross-linked PVOH. Several publications on PVOH with fillers, such as cornstarch [78, 79, 80] can also be found, although the purpose is most frequently for thin films, and the fillers typically reduce the strength of composite materials.

The material characterization analyzes the effects of space radiation on materials to be used on spacecraft using OLTARIS (On-Line Tool for the Assessment of Radiation in Space). Additional testing of the neutron shielding effectiveness was also performed in the Neutron Radiation Exposure Facility at NASA Langley Research Center.

2. RADIATION MODELING IN OLTARIS

2.1 OLTARIS Overview

OLTARIS (On-Line Tool for the Assessment of Radiation in Space) is an internet-based modeling tool that uses HZETRN (High Charge and Energy Transport) for aiding the development and selection of radiation shielding materials [81, 82]. Developed primarily for space applications, OLTARIS allows several options to be selected for input based on previous GCR and SPE measurements. Calculations for space radiation effects on electronics and biological systems are also possible using OLTARIS.

The radiation shielding in OLTARIS is determined from GCR and SPE radiation, mostly protons, electrons, and heavy ions and accounting for the secondary neutrons generated through atomic collision. For this research, the shielding of neutrons was determined experimentally using an Americium/Beryllium source. Therefore, it should be expected that there will be differences in the modeled and measured data. The reason for selecting OLTARIS was fourfold:

- OLTARIS accounts for the secondary radiation (neutrons) and backscatter.
- to determine radiation shielding performance expected in a realistic (space) radiation environment.
- to have output data (i.e. mSv/day) that can be compared to the experimental data.
- the polymers being modeled will be within an aluminum-hulled spacecraft, making secondary (neutron) radiation shielding a significant challenge.

2.2 OLTARIS Uncertainties

Uncertainties in OLTARIS output stem from the current generation of radiation transport codes. Uncertainties in the external radiation environmental models, transport algorithms, and

nuclear and atomic physics models contribute to non-biological uncertainties and are estimated to be about 15% for GCR [83, 84]. Uncertainty predictions may be much larger for SPE spectra. However, similar models (i.e. HZETRN PHITS, MCNP, etc.) currently being used show only minor differences in data output [85]. OLTARIS is a dynamic model that is constantly being validated against a wider set of data as it becomes available.

2.3 OLTARIS Project Input and Output

The OLTARIS user will initially create a new project or modify one that was previously created. Under the "Materials" tab, there is a list of common materials that have been provided by OLTARIS, such as silicon, water, polyethylene, lunar and Mars regoliths, etc. PVOH and cross-linked PVOH were not in the list, so they were generated for this research by entering the chemical formula and density. The material can also be defined by the elemental mass percentage or the molecular mass percentage.

The user will then create a slab or a sphere. Although a sphere may be a more appropriate choice for GCR, for this research the slab was chosen as a better comparison for the experimental data, since the test samples are disks irradiated from one side. Slab input parameters are *Name*, *Comments*, *Units* (for slab depth), *Material*, and *Thickness*. Each material and thickness is a data point, so even for a slab of a single material, several layers should be defined to make a smooth plot. For this research, the aluminum slab consisted of 13 data points of various thicknesses to get a smooth plot. The first few thinner layers were spaced to capture the initial steep rise in the dose equivalent, while the 1 cm (thicker) layers were sufficient for plotting the nearly straight downslope of the graph. Where polymer backing layers were being investigated, an additional 12 layer thickness data points (1/2 mm thick) were used.

From the Projects tab, the user can enter the project name and description and mission-specific parameters. The chosen parameters for this research were determined for developing manned spacecraft radiation shielding materials that would be required for missions to the Moon, Mars, or long-duration missions. Table 4 is a list of the input parameters for both GCR and SPEs and the rationale for their selection.

Table 4. Selected Input Parameters for OLTARIS Modeling.

OLTARIS Input Parameter		Parameter Chosen	Reason for Selection
GCR	Environment	GCR (free space, 1 AU)	GCR is constant for manned spacecraft in deep space and can lead to chronic health conditions. Lunar Surface and Mars Surface GCR options were not relevant.
	GCR Model	Badhwar-O'neill 2014 (BON14)	Based on actual measurements from ballons and satellites, including NASA's Advanced Composition Explorer (ACE) spacecraft.
	Historical Solar Min/Max	2010 Solar Min	The most recent and extreme condition was chosen for future mission planning.
SPE	Environment	SPE (free space, 1 AU)	SPEs are an intermittent threat for astronauts in deep space and can exceed GCR radiation levels, potentially causing acute health conditions. Lunar Surface and Mars Surface SPE options were not relevant.
	Historical SPE	October 1989	The most recent SPE model option. This SPE happened during a solar minimum.
Mission Definition		Historical Solar Min/Max	Selected this option as opposed to entering a date or fitting parameter.
Mission duration in days		1	Neutron testing output is in mSv/day, so a 1 day mission can be compared with test data.
Save External Differential Flux...		No	The project was saved and can be regenerated if necessary.
Geometry		selected slab	Slab geometry most closely resembles the testing configuration: disc samples irradiated from one side.
Response functions		Dose Equivalent, ICRP 60	based on internationally accepted recommendations for protecting radiation workers and the public.

The 2014 Badhwar-O'Neill Galactic Cosmic Ray (BON14) model [86, 87, 88, 89] was chosen for the GCR model input into OLTARIS, since it is based on data measured from particle detectors on satellites and balloons for over 60 years. The Advanced Composition Explorer (ACE) launched in 1997 currently provides among the most comprehensive GCR measurements

to date [90]. The detailed description for the BON14 GCR model is described in NASA Technical Publication TP-2015-218569 [91]. BON14 numerically solves the Fokker-Planck differential equation to characterize particle transport in an ideal spherically symmetric heliosphere:

$$\frac{1}{r^2}\frac{\partial}{\partial \mathrm{r}}\left(r^2 V_S \mathrm{U}\right) - \frac{1}{3}\left[\frac{1}{r^2}\frac{\partial}{\partial \mathrm{r}}\left(r^2 V_S\right)\right]\left[\frac{\partial}{\partial \mathrm{T}}\left(\alpha T\, U\right)\right] = \frac{1}{r^2}\frac{\partial}{\partial \mathrm{r}}\left(r^2 \kappa \frac{\partial \mathrm{U}}{\partial \mathrm{r}}\right) \quad (5)$$

where r is the radial position in astronomical units (AU); T is the kinetic energy of the proton or neutron (nucleon) in MeV/n; $U(r, T)$ is the GCR flux (particles/sr·m^2·s·MeV/n), $V_s(r)$ the solar wind speed (≈ 400 km/s); κ(r, T) the particle diffusion coefficient tensor; and $\alpha(T) = (T + 2T_0)/(T + T_0)$, with T_0 being the rest energy of the GCR particle. The solution assumes that at a boundary distance $r = R$b, modulation of $U(r, T)$ is negligible, and therefore provides the boundary condition at $U(R_b, T) = U_0$ as a known quantity. The Badhwar-O'Neill 2010 Galactic Cosmic Ray Flux Model depicts the GCR flux over the period from 1955 to 2010. It uses the solution to the Fokker-Planck equation to determine the flux of GCR particles of a given charge, Z, as a function of energy. Fig. 4 shows the high-energy spectra, both measured and modeled, for phosphorus, iron, and oxygen, data that is typical of that used for all the elements from Li (Z=3) to Ni (Z=28) [92]. The NASA GCR Environment Model details the use of the BON14 model [93, 94] used for this research in OLTARIS.

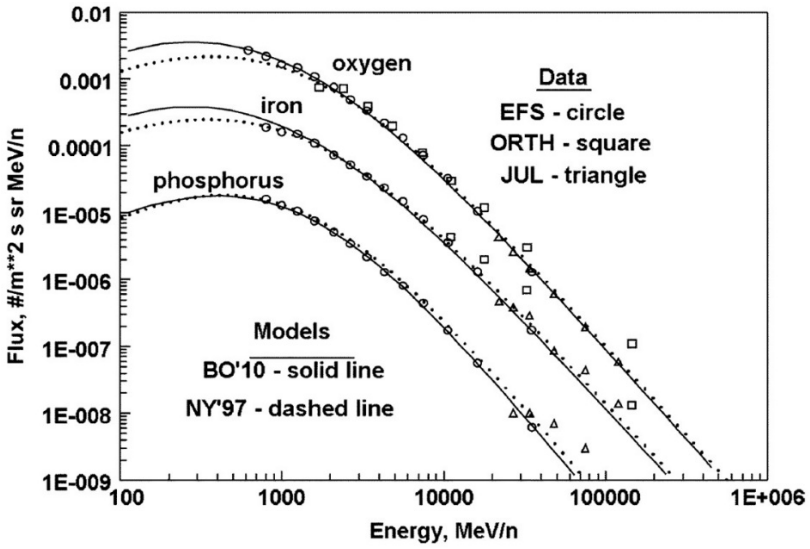

Fig. 4: The high-energy spectra for phosphorus, iron, and oxygen. (P.M. O'Neill)

The SPE chosen for this model was recorded in October, 1989. It was the most recent, and happened during a solar minimum, when the highest radiation levels occur. Again, the free space solar particle event environment at 1 AU was chosen. Each SPE option has a corresponding differential formula for modeling the radiation. Eqn. 6 is the radiation flux, ∅(E), for the October 1989 model:

$$\emptyset(E) \;=\; 6.33 \times 10^{8} exp\left(\frac{10-E}{12}\right) + 4.88 \times 10^{6} exp\left(\frac{100-E}{80}\right) \qquad (6)$$

NASA Reference Publication 1257 describes the October 1989 SPE [95], one of the largest in recent times, with particles 5 MeV–100 MeV energy range [96]. Although radiation levels for SPEs far exceed those of GCR, the duration of an SPE

The output for OLTARIS is selected by the user during the project setup. For this research, the *Dose Equivalent, (ICRP 60)* was the *Response Function* chosen, since the data would be compatible with the neutron testing data (mSv/day). ICRP 60 is a compilation of radiation protection recommendations for both radiation workers and the public. Other *Response*

Functions available are more appropriate for specific missions, such as astronaut health or examining the effect of radiation on tissue.

2.4 OLTARIS for GCR, Solar Minimum 2010

Input parameters for aluminum were determined, using an area density of 20 g/cm^2 to represent the spacecraft hull depth without secondary radiation shielding. The 20 g/cm^2 value is used frequently in the literature and corresponds to 7.4 cm thick aluminum, or a thickness accounting for the outer skin, insulation, inner skin, equipment, supplies, racks, etc. [97, 98]. The depth increment was variable to account for the initial increase in the dose equivalent, with the last point at 7.4 cm, or 20 g/cm^2 aluminum (see Fig. 5). The dose equivalents (mSv/day) for GCR were based on the GCR model (BON14) for free space at 1 AU and a one day mission duration.

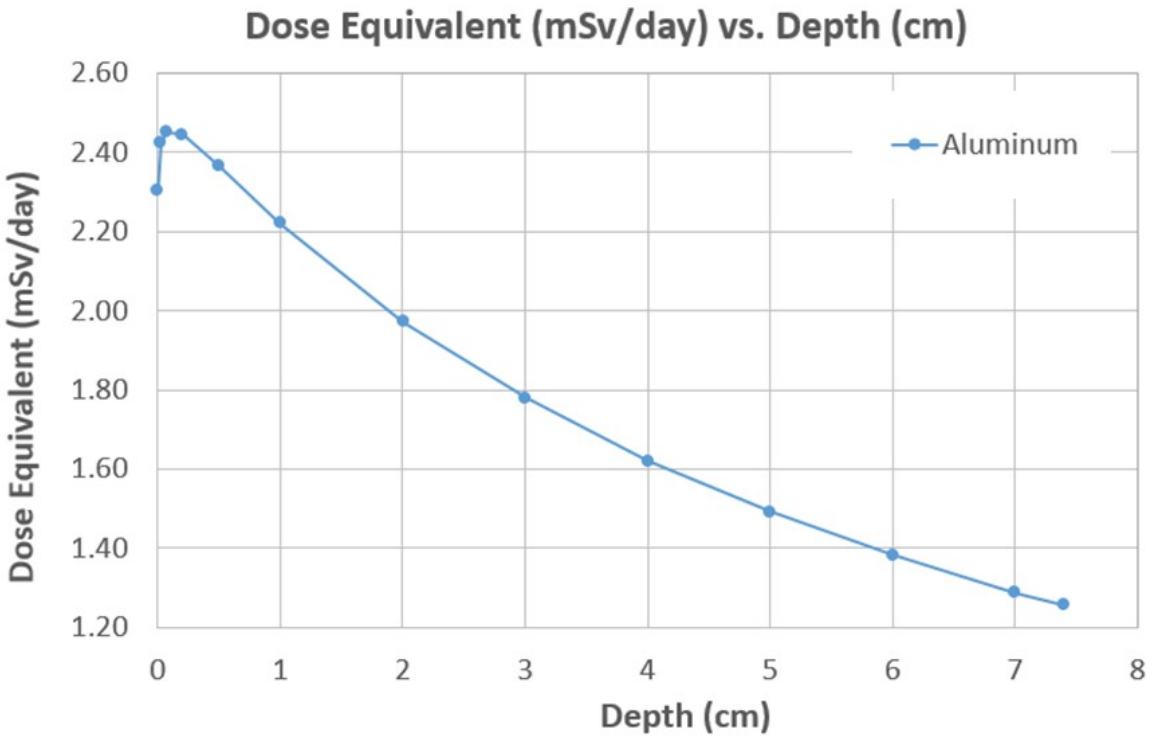

Fig. 5: OLTARIS - GCR dose equivalent in pure aluminum slab 7.4 cm (20 g/cm^2 thick).

For aluminum-hulled spacecraft of 20g/cm^2 depth, the GCR dose equivalent initially increased from 2.30 to 2.45 mSv/day at a depth of just 0.5 mm. The initial increase is due to scattering and the large flux of neutrons, gamma radiation, and ions produced from the primary GCR. The dose equivalent decreases after the 0.5 mm depth, reaching the initial BON14 GCR level at 0.75 cm depth and continues to a dose equivalent of 1.26 mSv/day at a slab thickness of 7.4 cm.

Fig. 6 shows the dose equivalent for 7.4 cm thick slabs of Aluminum, PVOH, cross-linked PVOH, and Polyethylene. After the 1.5 cm depth, the aluminum slab has the largest reduction in the dose equivalent.

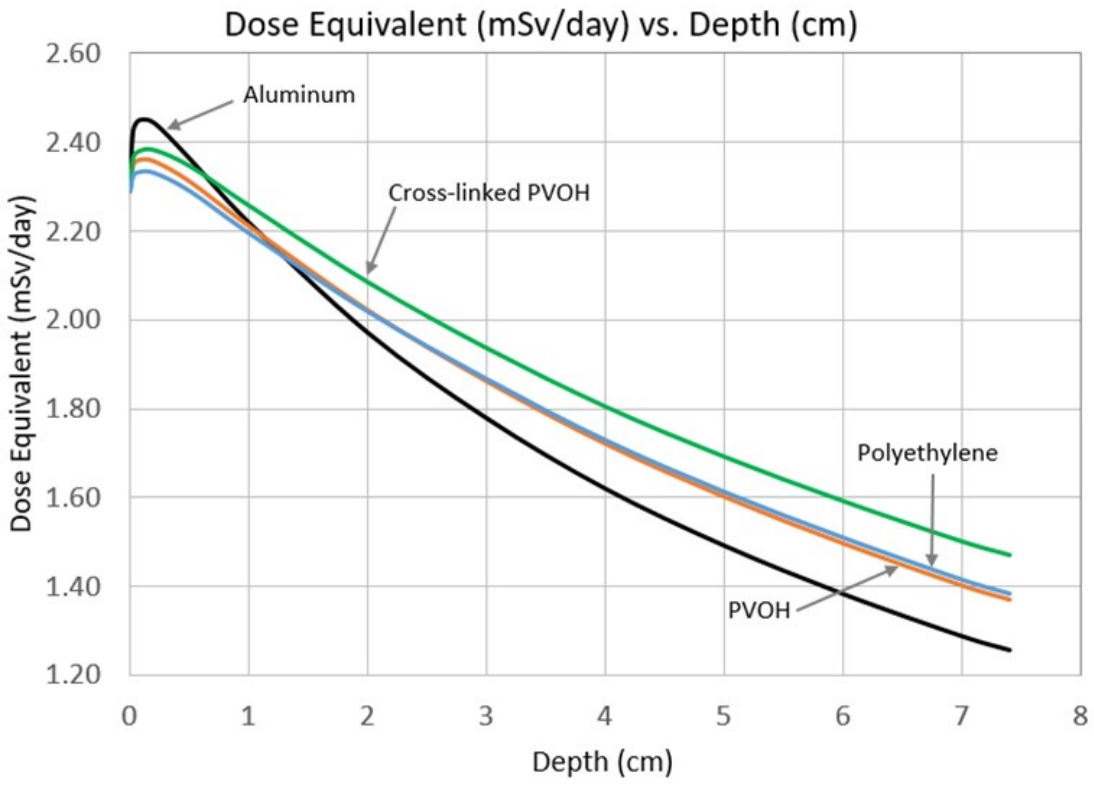

Fig. 6: OLTARIS - GCR dose equivalent of 7.4 cm thick slabs of Aluminum, PVOH, cross-linked PVOH, and Polyethylene.

The polyethylene and PVOH slabs have the same dose equivalent reduction, while the cross-linked PVOH has the least reduction, possibly due to the additional oxygen atoms involved in cross-linking.

The previous aluminum slab was modeled with an adjacent 6 mm thick layer of polyethylene. In this case, the cumulative thickness was 8 cm. Two additional configurations consisting of the aluminum layer backed by both a PVOH and a cross-linked PVOH layer were also run in OLTARIS. Fig. 7 shows an overlay of the dose equivalents for aluminum layers with polyethylene, PVOH, and cross-linked PVOH backing layers.

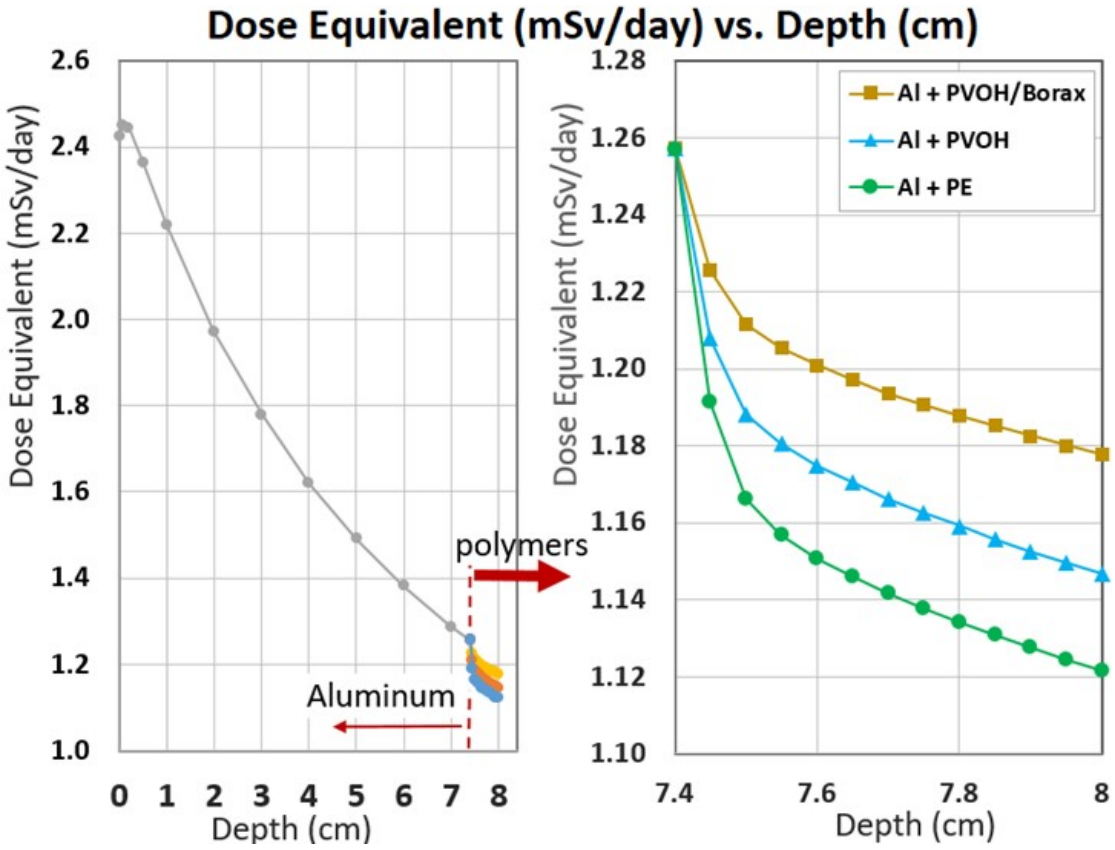

Fig. 7: OLTARIS - GCR dose equivalent in slabs consisting of an aluminum layer with a 6 mm thick polyethylene, PVOH, or cross-linked PVOH backing layer.

Compared to the aluminum slab, a sharper reduction in dose equivalent can be seen in all three polymer backing layers. The thickness of the 3 polymer layers, 6 mm, was chosen for comparison to the samples that were fabricated and tested for neutron shielding efficiency. It should be noted that the 7.4 cm thick aluminum layer is always included in the slab model, since the polymers are unsuitable for the primary spacecraft hull. For the case of the aluminum/polymer slab, there is no initial increase in the dose equivalent at the interface, since the polymers consist of atoms with lower atomic numbers than aluminum and are partially shielded from incident, higher energy GCR.

2.5 OLTARIS for SPE, October 1989.

Input parameters for SPE October 1989 were similar to the GCR parameters, except where GCR-specific input was replaced with the SPE input. Yearly dose calculation was not performed since SPEs last only hours or days. Percent efficiency is also not shown, since the dose equivalent is reduced beyond 1/1000 of a percent, making the daily shielded dose equivalent a better measurement for comparison. Initially, the shielding ability for 7.4 cm thick slabs of Aluminum, PVOH, cross-linked PVOH, and Polyethylene were compared (Fig. 8).

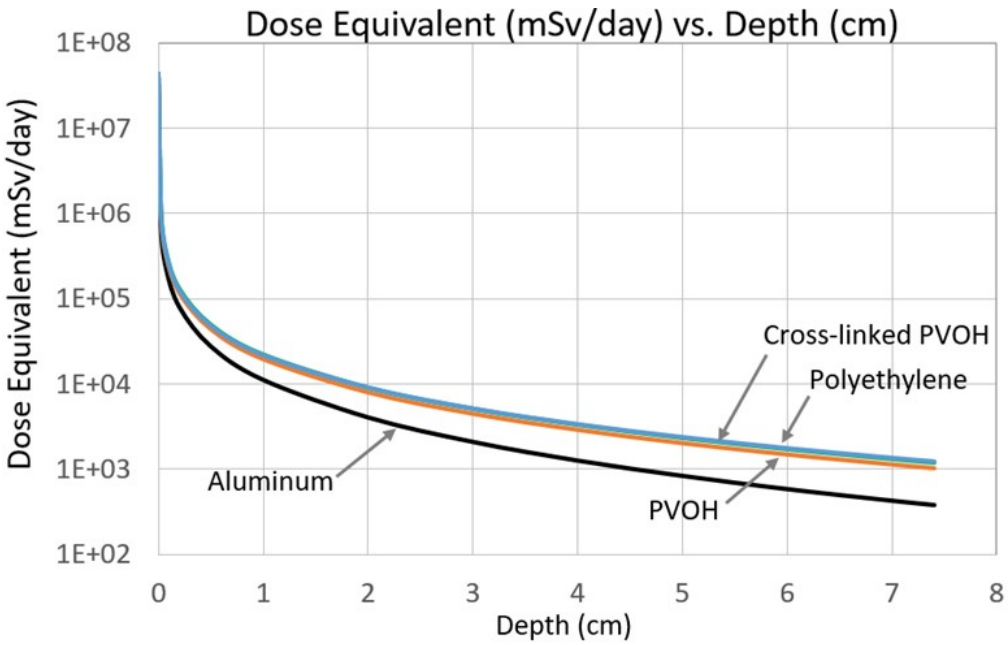

Fig. 8: OLTARIS - SPE dose equivalents of 7.4 cm thick slabs of Aluminum, PVOH, cross-linked PVOH, and Polyethylene.

In this case the initial SPE is $4x10^7$ mSv/day, with the greatest reduction in the aluminum slab to 382 mSv/day. The polymer slabs reduced the SPE dose equivalent to 1226, 1208, and 1030 mSv/day for the PE, cross-linked PVOH, and PVOH slabs, respectively. As with GCR, the aluminum slab had the largest reduction in dose equivalent.

The shielding ability of slabs consisting of 7.4 cm thick aluminum layers backed by 6 mm polymer layers is shown in Fig. 9.

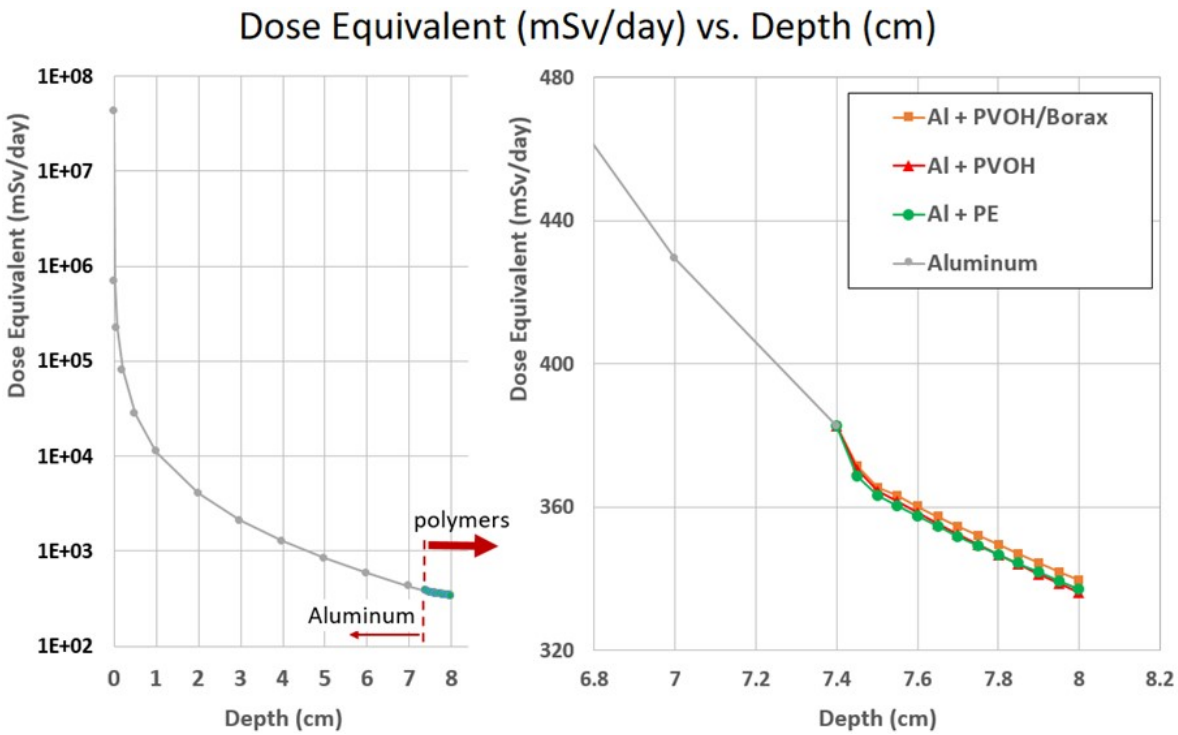

Fig. 9: OLTARIS - SPE dose equivalent in aluminum + polymer slabs.

The initial value of the dose equivalent in the aluminum layer for the 7.4 cm depth is 382 mSv/day. This was reduced to 340, 337, and 336 mSv/day for the cross-linked PVOH, PE, and PVOH, respectively.

3. SAMPLE FABRICATION

3.1 Preliminary Sample Fabrication

To investigate water-soluble materials that might be considered for neutron shielding, 25 samples were made from other materials (Table 5). Only non-toxic materials were considered. The structural requirements eliminated many of the materials that were fabricated. The PVOH with cotton fabric (predominantly cellulose) looked promising, but it was decided to focus on the PVOH and cross-linking it with borax since these are strictly the matrix material for composites.

Table 5. Preliminary Sample Fabrication, Selection Criteria, and Evaluation.

Sample Composition	Selection Criteria	Rejection Notes	No. of Samples
MDPE with 8 wt% BNNT	for comparison with other MDPE samples with less BNNT wt%	would not flow, raises the MP of the mixture well beyond that of MDPE	1
PVOH & cotton fiber	cotton is > 90% cellulose, good for composite, adds hydrogen	delamination and warpage, decided to focus on the PVOH matrix	6
PVOH & woven cotton (4-ply and 10-ply)	add cellulose for composite, woven for strength adds hydrogen	good composite, n-shielding dependent on drying, decided to focus on the PVOH matrix	2
PVOH with borax, dry and solution added, then mixed	adding boron for neutron absorption and crosslinking to improve PVOH strength	Immediate cross-linking, inconsistent distribution caused cracking and brittleness	6
PVOH with gypsum (calcium sulfate dihydrate)	added water (hydrogen)	too brittle and crumbled or easily cracked	2
PVOH with cornstarch	add hydrogen compatible with PVOH	extremely hard, exessive drying required, one developed mold.	3
100% Acrylic latex	water based (added hydrogen)	good composite, but too flexible, had other additives that might affect shielding	2
portland cement with borax powder and solution	add hydrogen (water) and boron (borax), comparison to similar, existing applications	too brittle and crumbled or easily cracked	3

3.2 Pure MDPE Sample Fabrication

Four pure-MDP samples were fabricated to be used as a baseline for determining neutron radiation shielding effectiveness. Medium density polyethylene (MDPE, Sigma Aldrich: 332119-500g) was used for all samples to be evaluated. The procedure for the pure MDPE required adding the MDPE powder (3 times the mold thickness) to the larger, 2.5-in (6.25-cm) diameter, copper mold (Fig. 10). The mold was then heated on a hotplate to 125 °C, the melting point of MDPE, until it turned clear and filled out the mold. A thin copper wire was used to remove any bubbles. The hotplate was turned off, allowing the sample to cool slowly to room temperature. The assembled mold was used to shave the excess MDPE off the top, using the sharp edge of a piece of metal sheet. This step ensures that all samples have the same thickness for the radiation shielding comparison.

Fig. 10: Copper sample molds: 2.5 in. and 1.375 in. diameters.

3.3 MDPE Composite Sample Fabrication

Five samples of MDPE/BNNT were fabricated for determining the effect of boron distribution for radiation shielding. The samples had BNNT weight percents of 4, 2, 1, 0.and two 0.5 (both diameters). BNNTs were measured for making ALL of the MDPE/BNNT samples, put in a 100-mL beaker, and ethanol was added to the 40 mL mark. A small stirring bar was added and the mixture was mixed on a hotplate at room temperature using the magnetic stirring feature until the BNNTs were fully dispersed (about 3 hours). To efficiently disperse the BNNTs, the beaker was moved until the spinning stirring bar was off-centered (near the side) within the beaker. Once dispersed, an amount of MDPE powder was measured to give the mixture the highest BNNT wt %, 4% for this research. The rationale was to fabricate all 5 samples from the same BNNT batch/process for uniformity, adding MDPE as each sample was made for successively lower BNNT wt % concentrations. The mixture formed a thick slurry that filled the mold, allowing excess to account for shrinkage once the ethanol evaporated. The smaller mold is to conserve BNNTs for samples with higher weight percent. The mold was then heated to 50 °C until the ethanol evaporated. The slurry was added until the dried amount could fill the mold, then the temperature was increased to 125 °C to melt the MDPE and make the sample. The sample was then weighed BEFORE trimming to determine the amount of MDPE to add for the next lower BNNT wt% concentration. These calculations were determined in an Excel spreadsheet for all composite samples fabricated. The sample was then trimmed to the mold thickness of 2 mm. The remaining samples were made following the same procedure, adding MDPE to make the 2%, 1%, and ½ wt% BNNT samples.

3.4 PVOH Sample Fabrication

The PVOH samples required a solution of 10 wt% PVOH chips in deionized water. A mixture was prepared using 80 grams of PVOH chips in 720 grams of deionized water in a 1 L Nalgene bottle. The bottle with the mixture was heated to 90 °C in a microwave oven for 2 minutes. The bottle was shaken for 1 minute, the top was briefly loosened to release pressure, then reheated in the microwave for an additional minute. The heating times vary depending on the microwave that is used and the power settings. The process was repeated as necessary to prevent the chips from melting together instead of dissolving into a smooth, viscous solution. The solution was then poured in the mold (Fig. 11) to a level twice the desired thickness of the finished sample.

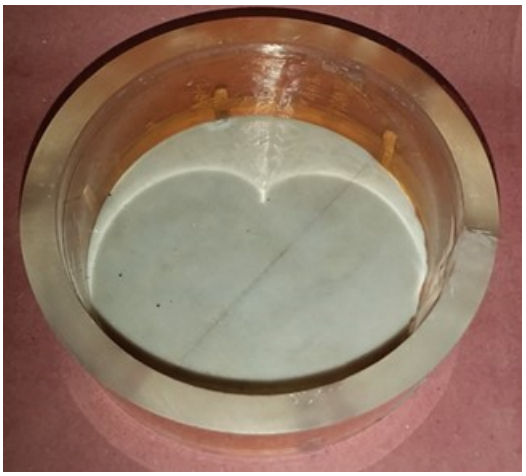

Fig. 11: Mold for PVOH samples.

Any bubbles were skimmed off the top of the surface and the mold was placed in the freezer to promote polymerization. The solution was frozen for a few hours; the time for polymerization dependent on the thickness of the samples. The freeze gelation process performs two purposes: polymerization of the PVOH and freezing (expansion) of the water. If allowed to thaw the

process results in a hydrogel. However the mold was put under an infrared heat lamp (GE, 250W) to evaporate the water until thawed (still gelled). A heat lamp was chosen as the method of heating the sample since it heats the bulk of the sample rather than just a surface. Deionized water was sprayed on the top surface periodically to prevent the sample from drying out and the top surface and the sample was flipped to prevent warping or uneven evaporation. Once the sample reached about 60 °C it was refrozen, and the previous process was repeated. Depending on the sample thickness, several iterations of this process were required to produce a rigid, dry sample. The amount of water remaining is indicated by the translucency: hydrated samples are opaque white, while dried samples are transparent to translucent.

3.5 Cross-Linked PVOH Sample Fabrication

Samples of PVOH cross-linked with Borax (20 Mule Team) were also fabricated. A 5 wt% Borax solution was first prepared by mixing the Borax in deionized water at 60 °C. A PVOH sample was allowed to thaw to the gel state, then submerged in the room-temperature Borax solution for 3 hours. The sample was then submerged in deionized water for 2 hours to allow the sodium ions and unreacted borate ions to diffuse into the water solution. After partially drying the cross-linked PVOH sample, it was refrozen, and the drying process used for the pure PVOH was initiated.

4. MATERIALS CHARACTERIZATION

4.1 Materials Characterization Using Infrared Spectrometry

4.1.1 FTIR background. Fourier Transform Infrared (FTIR) Spectroscopy is used to identify the chemical bonds and functional groups present in a material. The chemical bonds are identified by the specific wavelengths of infrared radiation that are absorbed. The Fourier transform converts the interatomic vibrations into an absorption frequency spectrum, expressed in wavenumbers (cm^{-1}). The interatomic vibrations are dependent on the masses of the atoms involved and their bond length. The vibrations can be in stretching or bending with the absorption of infrared radiation. The stretching mode is usually associated with the stronger peaks of functional groups, while the bending absorption mode usually indicates similar bond types. A shift in the frequency peak to a higher frequency indicates a decreased bond length, while a shift towards lower frequencies indicates the bond length increased.

FTIR spectra usually have a wavenumber range of 4000 - 400 cm^{-1}, frequently considered the mid-infrared region. Often the functional groups are initially identified in the wavenumber region of 4000 - 1500 cm^{-1}, since functional groups normally display the highest peaks. The higher peaks are due to the number of the particular bond types in the molecule and the polarity of the molecule. The 1500 - 400 cm^{-1} range often indicates more complex vibrational or bending modes, sometimes involving more than one bond. Due to the abundance and complexity of peaks in this region, identifying the source of the absorption peaks requires comparison to published IR spectra for known materials. Unique and prominent patterns of the peaks in this region can help to identify the bonding involved. The mass of atoms involved in bonding can

also give a clue toward identification; the larger the masses involved, the lower the IR frequency that is absorbed.

The Nicolet iS5 FTIR Spectrometer was used for all absorption spectral data in this research. FTIR was selected since PVOH has many hydroxyl groups, so the O-H peak in the IR spectra will show a broader and less prominent peak with borate anion cross-linking. The cross-linking be indicated by an O-H shift to a higher frequency.

4.1.2 FTIR Spectra of PVOH Sample to Determine Borax Cross-Linking. Infrared absorption spectras were obtained for samples of Borax powder, pristine polyvinyl alcohol (PVOH), and PVOH cross-linked with Borax for determining the presence of borate cross-linking. An initial comparison of three infrared absorption spectra was made to determine the presence of the borate anion involved in cross-linking PVOH. The samples were a pristine PVOH sample $(C_2H_4O)_n$, and a PVOH sample cross-linked with Borax ($Na_2B_4O_7 \cdot 10H_2O$), tested on the top and bottom surfaces. The infrared absorption spectra for the pristine and both sides of the Borax cross-linked PVOH sample are shown in Fig. 12. The peaks for some common functional groups (O-H, C-H, and C=O) were also labeled.

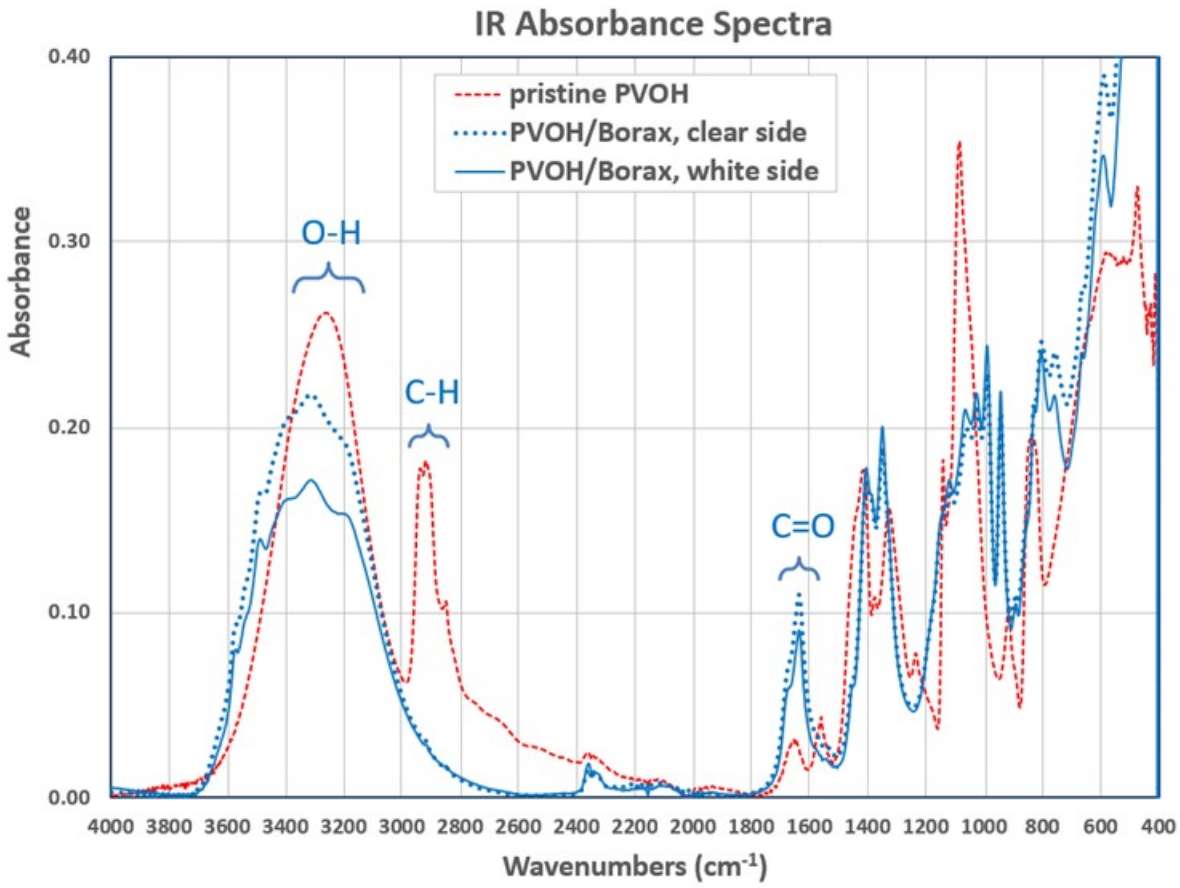

Fig. 12: Infrared absorbance spectra for pristine PVOH sample and both sides of a cross-linked PVOH sample.

Efflorescence of the Borax was present on the top surface of the PVOH / Borax cross-linked sample, and to a lesser extent on the bottom side. Therefore, the top side crust was shaved off to the original PVOH sample surface, and the before-and-after spectra were compared (Fig. 13). The same absorption peaks indicate the remaining presence of the borate anion in the bulk of the sample.

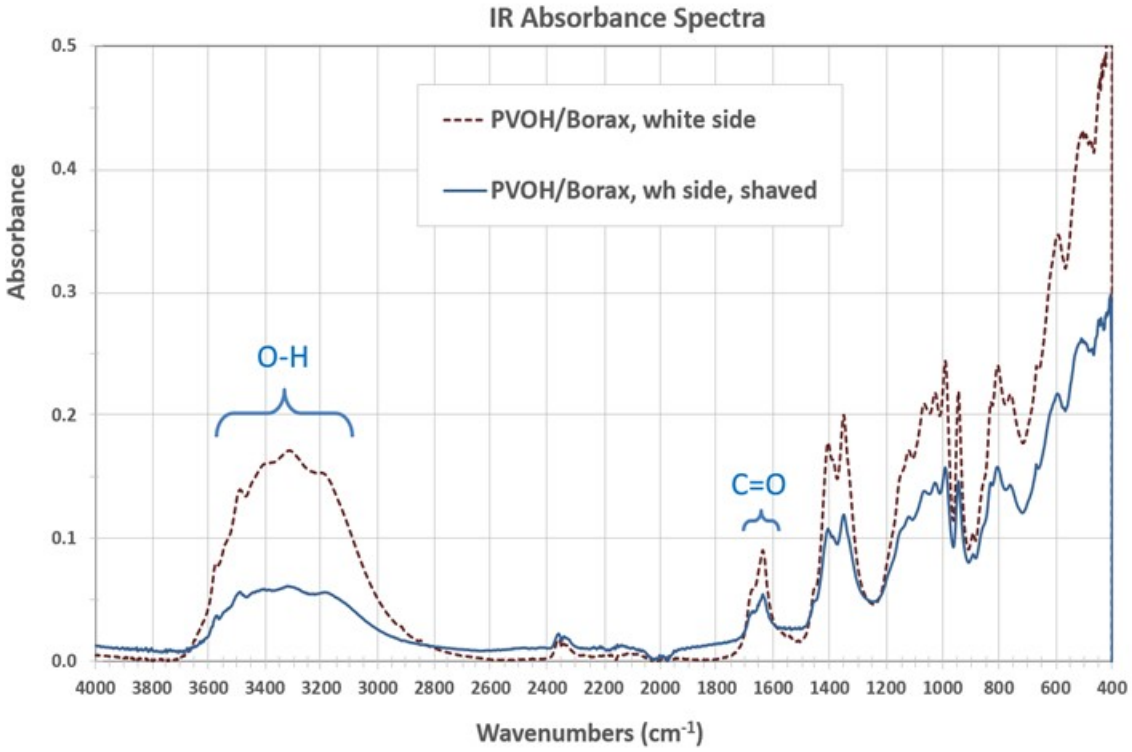

Fig. 13: Absorbance spectra for the top surface of the PVOH/Borax sample, before and after removal of excess Borax on the surface.

Both PVOH and Borax contain water. Borax ($Na_2B_4O_7 \cdot 10H_2O$) can also be converted to Tincalconite ($Na_2B_4O_7 \cdot 5H_2O$) under dry or hot conditions. The NIST Webbook database for chemistry has the IR absorption spectrum for Tincalconite, but not for Borax [99]. Spectra for both, using the SensIR Durascope on a Nicolet Magna 860 FTIR, was found in the RRUFF Project database (http://www.rruff.info/.com) and compared [100]. The peaks were identical for Tincalconite and Borax, suggesting that the two cannot be distinguished from one another using infrared absorption wavenumbers. A higher absorption along the entire spectrum for the sample cross-linked with Borax, however, can likely be attributed to the higher water content.

To isolate the IR absorbance due only to borax, the IR spectrum for pure borax powder was compared to previous data collected by C.E. Weir of the National Bureau of Standards, renamed

the National Institute of Standards and Technology (NIST) [101]. The published data indicates numerous similar absorption peaks for Tincalconite and borax (Table 6). Compared to the spectra in this study, the peaks showing the most similarity are with the Tincalconite. It should be noted that all materials were dry, and that the cross-linked PVOH samples were prepared from solution and then dried. For the cross-linked samples, the borax peaks may be shifted and broadened due to the hydrogen bonding and the resulting absorption resonant modes. The borate anion spectrum was determined to occur in the 1,200 – 400 cm^{-1} wavenumber range.

Table 6. FT-IR Absorption for Tincalconite and Borax. Both (a) and (b) from C.E. Wier and (c) Measurements Performed for This Study.

Tincalconite and Borax Absorption Spectra (cm^{-1})		
Tincalconite $Na_2B_4O_7 \cdot 5H_2O$	**Borax** $Na_2B_4O_7 \cdot 10H_2O$	**Borax powder** (*measured*)
(a)	**(b)**	**(c)**
3500 sb	3500-	3500
3340 vsb	3000 vsvb	3342
3000 svb		3020
2400 svb	2000 svb	2000
1630 mvb	1620 mvb	1654
1455 msh	1450 msh	1420
1405 svb	1390 svb	
1340 vsvb	1330 vsvb	1339
1190 msh	1275 mvb	1251
1155 sb	1155 mb	
1125 svb	1123 mvb	1129
1075 svb	1070 mb	1075
1025 svb		
985 sb	980 sb	991
940 sb	935 sb	941
805 sb	800 svb	817
750 mvb	750 svb	770
665 mvb	665 mvb	676
600 mvb	595 wb	606
520 mvb	505 mshvb	521
425 mvb	420 sb	425
	395s	

The pristine PVOH spectrum, as shown in Fig. 14, was compared to the shaved, cross-linked PVOH. The absence of the C-H bond peak in the shaved cross-linked PVOH sample is another indicator of cross-linking, due to the hydrogen bonding of the borate anion.

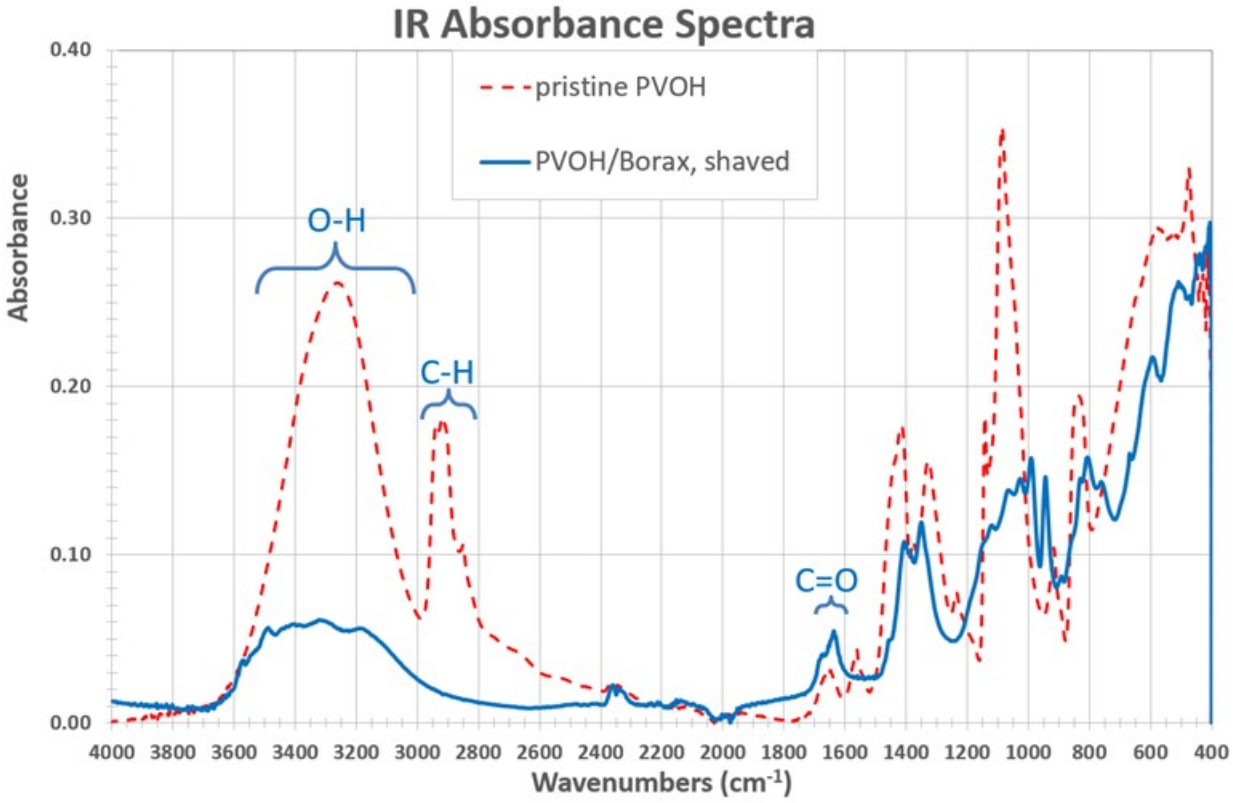

Fig. 14: Absorption spectra for pristine PVOH and shaved, cross-linked PVOH sample.

The absorption peaks were tabulated (Table 7) and compared to that of powdered borax. Identical peaks were highlighted for borax, PVOH, and the cross-linked PVOH. Both the lack of matching wavenumbers and the peak broadening in the alcohol (OH) group, 3200 – 3600 cm-1 range, strongly indicate the presence of borate bonds. Chemically, the crosslinking of PVOH with borax can result in other hydrogen bonds with water and the hydroxyl groups from adjacent PVOH chains as seen in Fig. 15. It is these bonds that make it difficult to quantify the actual amount of borate anion in cross-linked samples.

Table 7. Infrared Absorbance in Borax, PVOH, and Cross-Linked PVOH.

Absorbance Spectra Wavenumbers (cm^{-1})		
Powdered Borax $Na_2B_4O_7 \cdot 10H_2O$	**PVOH** $(C_2H_4O)_x$	**Borax Cross-linked PVOH**
3500	3258	3488
3342	2938	3321
3000	2918	
	2850	
2360	2360	2360
2341		2341
2117	2122	2002
1654	1654	1637
	1560	
1420	1415	1406
1377	1377	
1339	1328	1350
1251	1236	
1129	1086	1120
1075		1066
		1027
991		991
941	916	944
818	835	892
770		807
704		762
606		668
	574	594
	524	508
459	474	447
	428	438
425		425

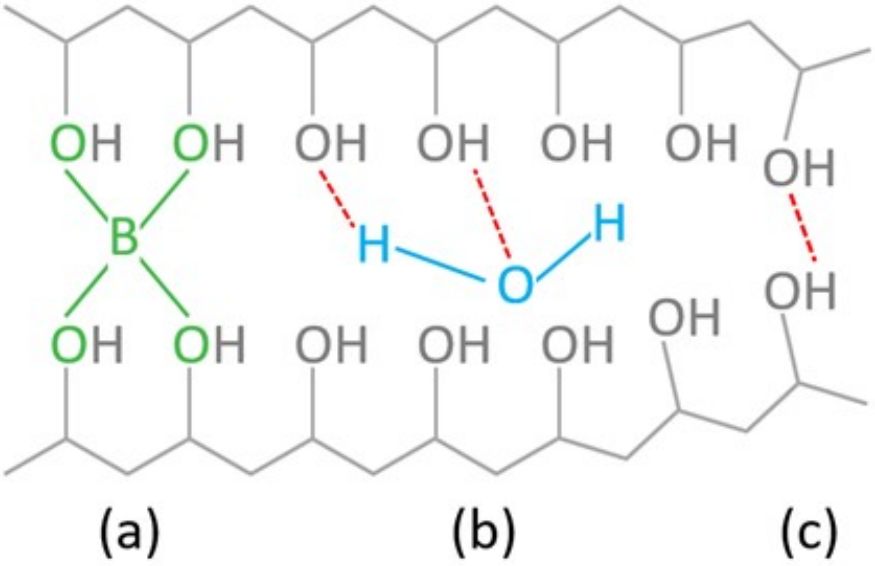

Fig. 15: (a) Borax cross-linking, (b) hydrogen bond with a water molecule, and (c) with hydroxyl groups.

Cross-linking PVOH with borax not only improves the structural properties of the composite, but results in an improvement in the radiation shielding properties. Neutron radiation shielding tests comparing the borax cross-linked sample to the pristine sample showed 2% improved shielding for the cross-linked sample, even though the area density was only 0.3 g/cm^2.

The comparison of the FTIR spectra for pristine and cross-linked PVOH reveals the broadening and the left-shifted O-H peak, indicating the presence of chemically bonded borate anions. The comparison of powdered borax FTIR peaks to the cross-linked PVOH sample revealed 4 peaks not present in the pristine PVOH sample: wavenumbers 2341, 991, 944, and 425 cm^{-1}. This verifies that the O-H broadening and the left shift is not merely due to water or the hydroxyl groups. Although the hydrogen atoms in PVOH make an excellent, stable method for moderating neutrons, the boron atoms (boron-10) have the high radiation cross section for capturing thermal neutrons. It could be seen from the neutron shielding improvement and the

FTIR spectral analysis that borax cross-linked PVOH would be a cheap, effective neutron shielding material.

4.2 Neutron Radiation Shielding Characterization

4.2.1 Neutron exposure equipment and configuration. For neutron radiation shielding characterization, an Americium-Beryllium (AmBe) neutron source with an ionizing radiation of 1 Ci was used in combination with a Ludlum Model 2363 gamma-neutron survey meter and Model 42-41 neutron probe.

The AmBe source has an average neutron energy of 4.30 MeV and a maximum dose equivalent of 384 pSv cm^2 [102]. The survey meter (see Fig. 16) was connected to a pc for data recording.

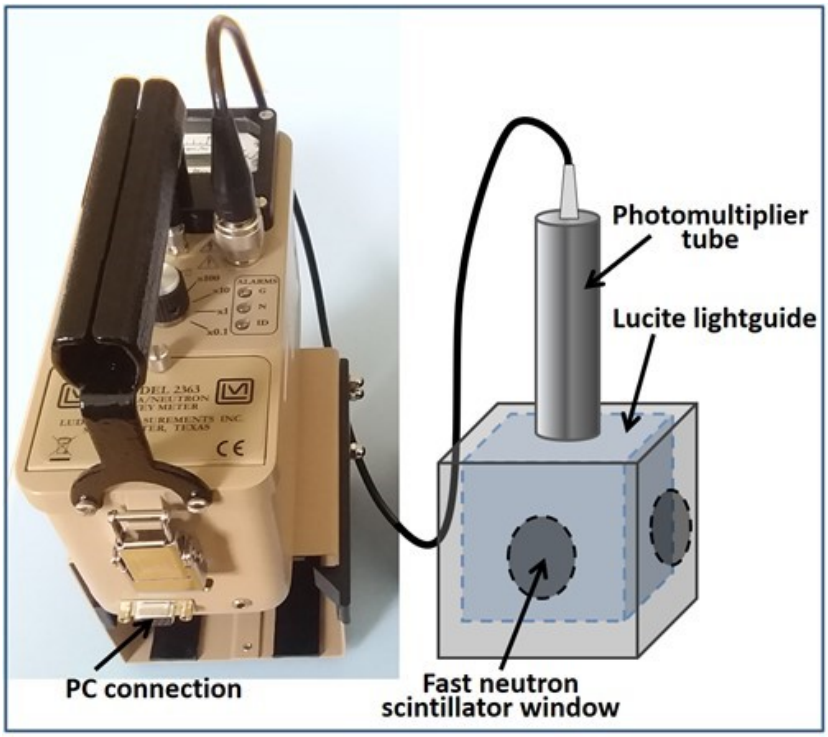

Fig. 16: Gamma-neutron survey meter and neutron probe.

The neutron probe consists of 4 fast neutron scintillators arranged around a Lucite light guide. As the neutrons from the source collide with the protons in the window material, the

protons recoil and strike a scintillating material to generate optical photons. A photomultiplier tube within the handle centered on the top face detects the photons coming through the light guide [103]. The real-time data collected for this study was in mrems/hr, then converted to mSv/day (mrems/hr x 24 hrs/day x 0.01 mSv/mrem) for comparison to literature and the OLTARIS data collected. The slab geometry (rather than spherical) was selected for OLTARIS as a comparison to the sample testing since it is a through-the-thickness measurement, and similar to the testing setup. Fig. 17 shows the configuration for neutron radiation exposure. The sample holder is adjustable to hold various sample sizes.

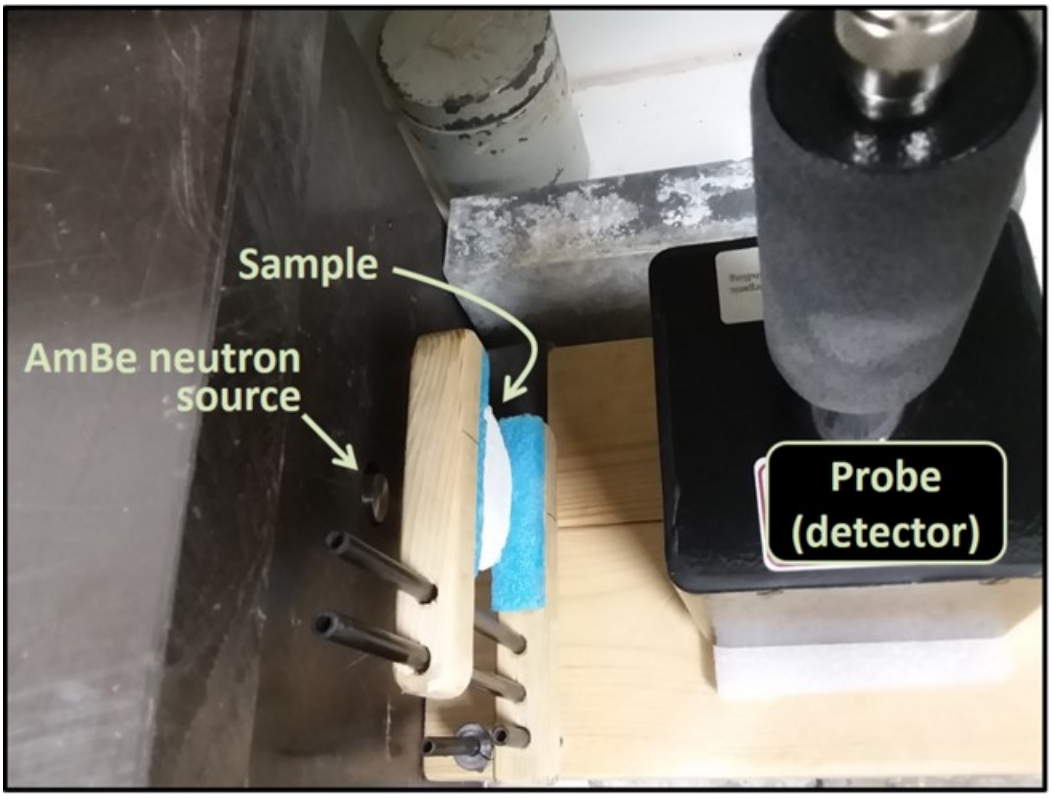

Fig. 17: Neutron exposure configuration.

The AmBe source, the sample, and the probe were aligned. Although the distances between each are adjustable, all data for this study was from a source-to-sample distance of 5.1 cm (2 in.) and a source-to-probe distance of 11.4 cm (4.5 in.).

4.2.2 Sample measurement and measurement uncertainties. Data was collected each second for 4 minutes (240 measurements) for each sample. A mean average was used for the dose equivalent, and the standard deviation was also determined. Neutron shielding tests were first performed on the PE/BNNT samples with different weight percentages of BNNTs. Three stacked samples were tested, consisting of 1, 2, and 4 wt% BNNTs in a polyethylene matrix, the testing configuration as shown in Table 8. Two orientations for 3 PE/BNNT stacked samples were tested. Each sample was approximately 2 mm thick, for a total thickness of 6.01 mm. The first orientation was with the 4%BNNT facing the neutron source, followed by the 2% and 1% BNNT samples. The first, with a neutron dose equivalent of 28.93 mSv/day shielded 7.97% of the neutron flux. The stack was then flipped around with the 1% BNNT sample facing the source. For this configuration, a dose equivalent of 28.72 mSv/day was measured, 8.64% shielding of neutrons. The result suggests that the boron concentration is more effective the further it is from the source, since neutrons lose energy as they propagate through the thickness, and since the boron-10 in BNNTs are more effective at thermal energies.

Table 8. Two Orientations for PE/BNNT Stacked Sample Testing.

Sample ID	Depth (mm)	Neutron Dose Eq (mSv/day)	shielding percent	Description
S421D	6.01	28.93	7.97	3 MDPE/BNNT stacked: Source → 4 → 2 → 1 wt% BNNT
S124D	6.01	28.72	8.64	3 MDPE/BNNT stacked: Source → 1 → 2 → 4 wt% BNNT

Neutron radiation shielding efficiencies were then determined for samples consisting of MDPE (the control sample), PVOH, and PVOH cross-linked with borax.

A measurement of 31.43 mSv/day was taken without a sample installed. This was the initial neutron radiation dose equivalent measurement that was compared to all sample measurements to determine the dose equivalent coming through each sample and the percent shielding. Due to the small differences in dose equivalent and the standard deviation for each measurement, error analysis was performed on the *no sample* setup as shown in Fig. 18. This condition was analyzed to find errors in the AmBe source and detector configuration (without a sample) to determine the acceptability of using a mean average for all measurements as opposed to using the median average. The difference in the mean and the median average was 0.071 mSv/day, allowing the mean average to be used for all measurements.

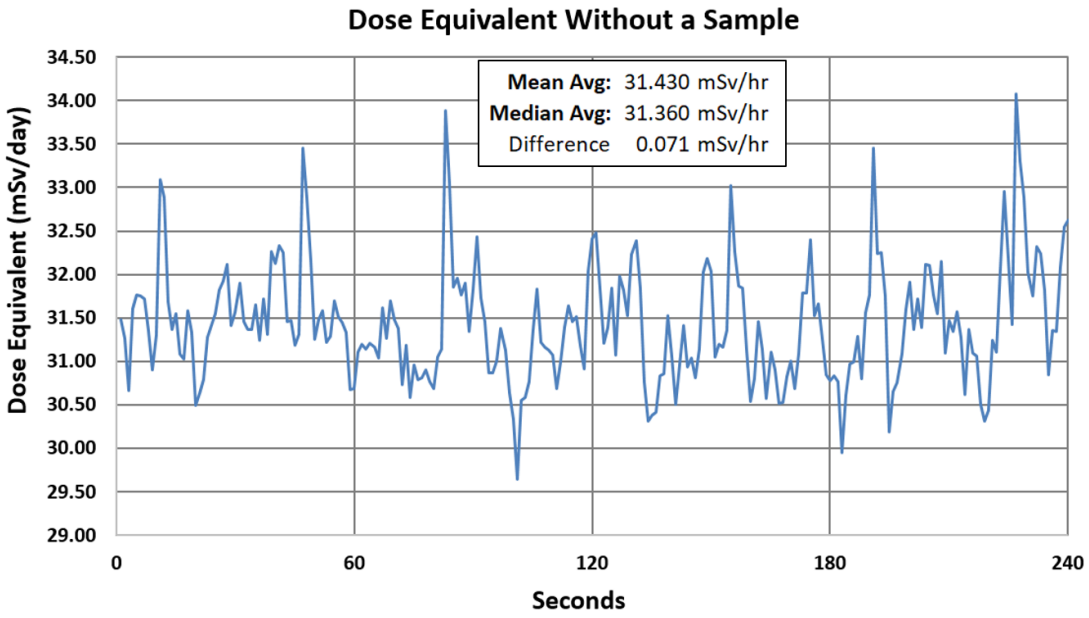

Fig. 18: Mean average dose equivalent (mSv/hr) for the *no sample* measurement.

The measurement duration was also analyzed to determine the minimum measurement time required to minimize the deviation from the mean average, as shown in Fig. 19. After a 2 minute duration, the difference in the dose equivalent measurement varied by 0.04 mSv/day (31.43 – 31.39), suggesting that the 4 minute measurement period was sufficient for sample measurement and comparison.

AmBe Source Measurements (no sample)		
Measurement duration (min)	Dose Equivalent (mSv/day)	Std Dev (mSv/day)
0.5	31.48	0.57
1.0	31.56	0.58
1.5	31.50	0.62
2.0	31.42	0.63
2.5	31.41	0.62
3.0	31.39	0.62
3.5	31.39	0.63
4.0	31.43	0.68

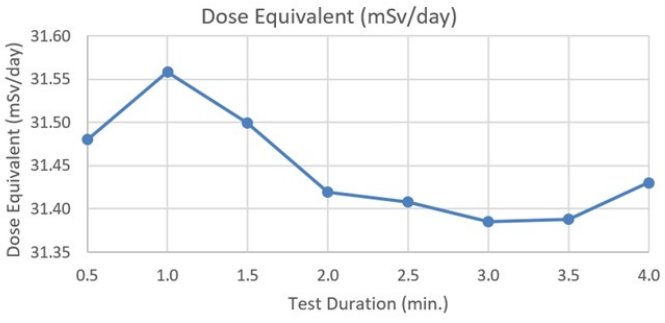

Fig. 19. Mean average dose equivalent (mSv/hr) for a testing duration of 0.5 to 4 minutes.

The standard deviation for the 4 minute exposure without a sample was then compared to the standard deviation for all sample measurements. The standard deviation for the "no sample" measurement during the 4 minute exposure was 0.68 mSv/day. The standard deviation range for the sample measurements was between 0.58 and 0.75 mSv/day, with an average standard deviation of 0.65 mSv/day. This suggests that the majority of uncertainties in sample measurement are due to the AmBe source and detector, with minor variance in the sample measurements.

5. DISCUSSION

5.1 Comparison of OLTARIS Results

Table 9 shows the reductions in dose equivalent (from GCR incident radiation) for 7.4 cm thick slabs of each material and 8 cm thick slabs consisting of aluminum layers backed by polymer layers representing the shielding added to the spacecraft interior. For the 7.4 cm thick slabs of each single material, the PVOH and the polyethylene reduce the dose equivalents by 40.1 and 39.6%, respectively. The cross-linked PVOH slab reduces incident GCR radiation by 35.8% and the aluminum slab by 45.5%. The higher reduction in the 7.4 cm thick aluminum is the result of the higher atomic number. The larger atoms produce more collisions with the high energy protons and core atoms that are abundant in GCR. However, the collisions also produce secondary radiation and neutrons. The secondary radiation is more effectively reduced with the hydrogen atoms (of polymers). This is evident in the abrupt decrease in the dose equivalent at the aluminum/polymer interface: 0.09 (polyethylene), 0.07 (PVOH), and 0.05 (cross-linked PVOH) mSv/(day·mm) from 0.01 mSv/(day·mm) in aluminum.

Table 9. OLTARIS - GCR Shielding for Solid 7.4 cm Thick Slabs and 8 cm Thick Aluminum/Polymer Slabs.

GCR Dose Equivalents in 7.4 cm thick slabs

	Al only	PE	PVOH	PVOH/Borax
daily reduction :	1.05 mSv/day	0.91 mSv/day	0.92 mSv/day	0.82 mSv/day
dose equiv for 6 mo. :	459 mSv	505 mSv	501 mSv	537 mSv
% Reduction per day :	**45.5 %**	**39.6 %**	**40.1 %**	**35.8 %**

GCR Dose Equivalents in Aluminum + Polymer slabs

	Al only	Al + PE	Al + PVOH	Al + PVOH/Borax
Total Thickness :	7.4 cm	8 cm	8 cm	8 cm
daily reduction :	1.05 mSv/day	1.18 mSv/day	1.16 mSv/day	1.13 mSv/day
dose equiv for 6 mo. :	229 mSv	205 mSv	209 mSv	215 mSv
% Reduction per day :	**45.5 %**	**51.3 %**	**50.2 %**	**48.9 %**

The largest reduction in dose equivalent is in the slab with the 7.4 cm thick aluminum layers backed by a 6 mm thick polyethylene layer, with a total reduction of 51.3% in the dose equivalent. The PVOH-backed aluminum slab shows a similar slab reduction of 50.2%. The aluminum with the cross-linked PVOH slab had a 48.9% reduction, only 3.4% better than the aluminum slab alone. At thermal energies, the boron-10 in the cross-linked sample becomes the most effective for neutron capture. Although the data shows the lowest reduction for the PVOH/Borax, a slab thicker than 6 mm may show better performance. The modeling also considers all particle and photon transport energies, and the chemistry of each material.

Table 10 shows the reductions in dose equivalent from SPE incident radiation for 7.4 cm thick slabs of each material and 8 cm thick slabs consisting of aluminum layers backed by polymer layers. For the 7.4 cm thick slabs of each single material, the aluminum slab showed the largest SPE dose equivalent reduction to 382 mSv from an initial value of 4.31 x 10^7 mSv/day.

Table 10. OLTARIS - SPE Shielding for Solid 7.4 cm Thick Slabs and Aluminum/Polymer Slabs.

SPE Dose Equivalents in 7.4 cm thick slabs *All slabs show reduction of* 4.31E+07 mSv/day

	Al only	PE only	PVOH only	PVOH/Borax
Thickness :	7.4 cm	7.4 cm	7.4 cm	7.4 cm
Initial SPE equiv. dose :	4.E+07 mSv/day	4.E+07 mSv/day	4.E+07 mSv/day	4.E+07 mSv/day
Shielded (remaining) :	**382** mSv/day	**1226** mSv/day	**1030** mSv/day	**1208** mSv/day

SPE Dose Equivalents Aluminum + Polymer slabs

	Al only	Al + PE	Al + PVOH	Al + PVOH/Borax
Total Thickness :	7.4 cm	8 cm	8 cm	8 cm
Shielded (remaining) :	**382** mSv/day	**337** mSv/day	**336** mSv/day	**340** mSv/day

Although the PVOH slab showed a higher dose equivalent reduction among the polymers, 1,030 mSv/day, it verifies the fact that aluminum is the most effective material for the initial reduction of SPE radiation, again due to the higher atomic number of aluminum being the most effective for scattering protons and core atoms in both GCR and SPE radiation. This does not imply that aluminum is all that is required for radiation shielding. The polymers are not as efficient at shielding high energy GCR, but are much better at shielding secondary neutron propagation. This fact becomes apparent with the modeling for the slabs with a 7.4 cm thick aluminum layer followed by a 6 mm thick polymer layer. Dose equivalent reductions for the aluminum/polymer-backed slabs show the greatest reduction in the aluminum/PVOH slab to 336 mSv/day. The aluminum/cross-linked PVOH and the aluminum/polyethylene slabs reduced the dose equivalents to 340 and 337 mSv/day, respectively.

Modeling GCR and SPE radiation transport in OLTARIS yielded small differences from the sample test data for the MDPE, PVOH, and cross-linked PVOH. It is not surprising, since the differences in shielding performance of the 3 polymers is small and the testing included data for only neutron shielding without consideration of proton and core atom radiation transport. The OLTARIS model accurately predicts the similar shielding ability for polyethylene and PVOH. The cross-linked model does not agree with the test result. A possible reason would be that OLTARIS calculates for GCR and SPEs comprised of protons and atomic nuclei and secondary neutrons in a range of energies, while the test data detects radiation from a neutron source only and within a narrow energy range. Additional consideration should be given for the amount of remaining water in PVOH after the drying process.

The SPE radiation, as modeled in OLTARIS, is several orders of magnitude higher than that of the GCR: 4.31×10^7 versus 2.30 mSv/day. For the four 7.4 cm thick aluminum and

polymer slabs, there is no initial increase in the dose equivalent, as scattering is the predominant shielding mechanism. For the polymer slabs, the PVOH had the highest reduction of dose equivalent to 1030 mSv/day, followed by cross-linked PVOH and PE, 1,208, and 1,226 mSv/day, respectively. The higher performance of the PVOH and cross-linked slabs may be due to the slightly higher atomic number of the oxygen atoms present in them and lacking in the polyethylene. The disparity in dose equivalent reduction narrows to within a few mSv/day, as shown the slabs with aluminum backed by polymer results. In these cases, the dose equivalent of 382 mSv/day for the aluminum layer is reduced to 336, 337, and 340 mSv/day in the PVOH, PE, and cross-linked PVOH layers, respectively. It is suggested that as the particle energy decreases, the remaining energy will reach a point where the bond energy is greater, and particle capture becomes the predominant shielding mechanism.

5.2 The Sample Fabrication Processes

The sample fabrication for MDPE requires the MDPE to be heated and formed in the mold. Variations of the process would still involve heating. A sample with 8% BNNTs was attempted, but did not flow and fill out the mold. The effort was abandoned since it would require a different forming process such as pressing. The PVOH samples used the freeze gelation process, and did not require heat. Although the process could involve heating the PVOH pellets, freeze gelation was chosen to maximize the polymer chain length for increased sample strength. Freeze gelation also lowers the density, since it is a xerogel once cured. For the cross-linked samples, freezing expands the structure to allow diffusion of the borax solution before the drying process. The combination of these processes was intended to prevent the cross-linking before the polymerization took place.

5.3 Neutron Shielding Characterization

Four samples of PVOH were tested: G1, G2, G3, and G4, as shown in Table 11. The first 3 were then stacked to determine the shielding for a 6 mm depth. A cross-linked PVOH sample, 190319wBx, was then tested.

Table 11. Neutron Shielding for PVOH, Cross-Linked PVOH, and Polyethylene Samples.

Sample Tested	Composition	Thickness (mm)	Dose Equivalent (mSv/day)	Std Dev (mSv/day)	Coeff of Variation (%)	Shielding %
no sample	NA	0.00	31.43	0.68	2.2	NA
G1	PVOH	1.40	30.15	0.63	2.1	4.1
G2	PVOH	2.00	30.13	0.63	2.1	4.1
G3	PVOH	2.60	30.16	0.69	2.3	4.0
G4	PVOH	2.00	30.22	0.59	2.0	3.9
G1+G2+G3	PVOH	6.00	28.61	0.62	2.2	9.0
190319wBx	PVOH/Borax	3.20	29.63	0.65	2.2	5.7
PE1	polyethylene	2.10	30.25	0.58	1.9	3.8
PE1+PE2	polyethylene	4.30	29.26	0.75	2.6	6.9
PE1+PE2+PE3	polyethylene	6.50	28.53	0.65	2.3	9.2

Three polyethylene samples, PE1 (2.1 mm thick), PE2 (2.2 mm thick), and PE3 (2.2 mm thick) were tested for comparison. PE1 was tested first, followed by two stacked samples (PE1+PE2), and three stacked samples (PE1+PE2+PE3). Neutron shielding percent for all samples is dependent on the depth (thickness). It is calculated using the "No sample" dose equivalent measurement and the test sample dose equivalent:

$$\frac{(no\ sample) - (test\ sample)}{(no\ sample)} \times 100$$

Normalization of the data would require several samples of each material to determine the non-linear neutron transport through the thickness. This is due to the increasing number of neutron scattering events with increasing depth. Therefore, the plot of dose equivalents as shown in Fig. 20, was used as a comparison of PVOH and cross-linked PVOH to polyethylene.

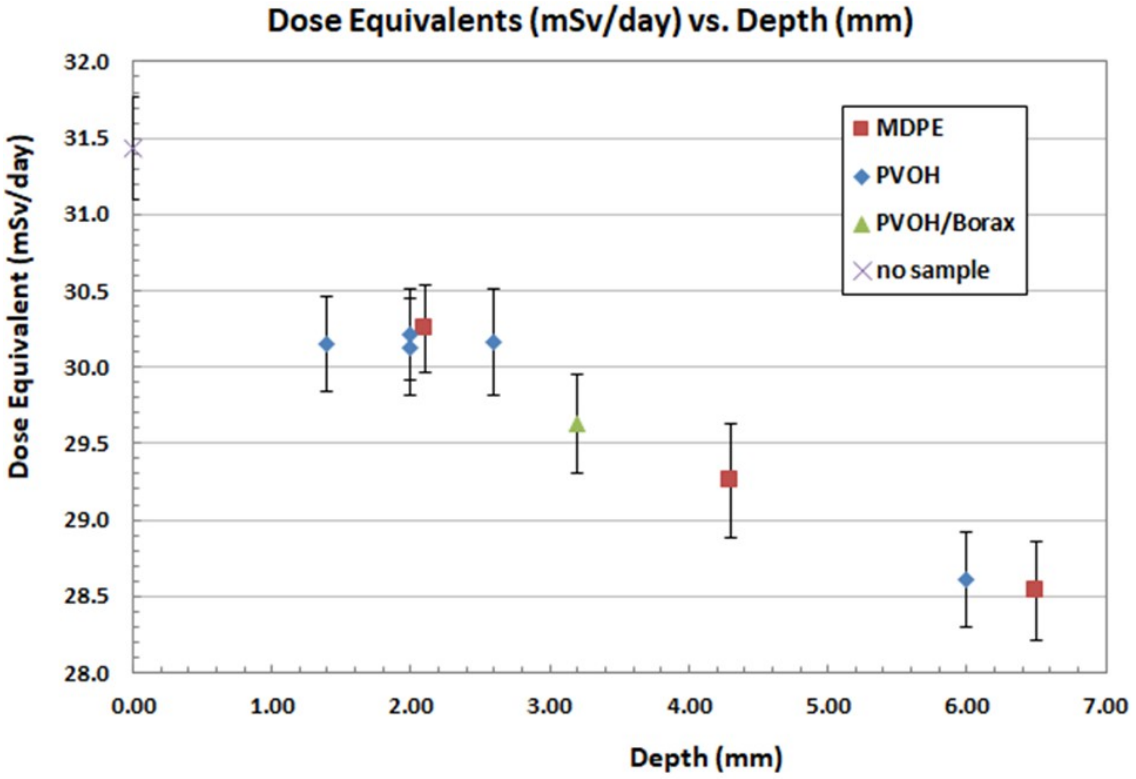

Fig. 20: Dose equivalent in MDPE, PVOH, and cross-linked PVOH samples.

All but one of the data points for PVOH appear below the MDPE curve, indicating a slightly higher reduction in dose equivalent for samples of thickness between 1.4 and 6.5 mm thick. The dose equivalent reduction implies that PVOH and cross-linked PVOH can be as effective as polyethylene, but with the advantage of using natural fibers such as cellulose as reinforcement in secondary structural composites. Samples G1 and G2, both 2 mm thick, vary by 0.09 mSv/day dose equivalent reduction. This could be due to a small difference in water content after the drying process.

6. CONCLUSION

The current plan for NASA astronauts to return to the Moon and land astronauts on the surface by 2024 will be followed by a permanent human presence on the surface. The lunar outpost will not only establish a lunar-based economy for the benefit of US companies and international partners, but will also be a starting point for a planned Mars mission. The long-duration missions beyond the Earth's protective magnetosphere will require radiation shielding systems to protect astronauts and electronic equipment in spacecraft, lunar or Mars habitats, and surface vehicles. Ionizing radiation from GCR and SPE's consist mainly of protons, heavy ions, and electrons. The interaction of these particles with the metal hull of spacecraft or other metallic structures produces secondary neutron radiation, potentially more damaging to human tissue than the incident radiation. An effective neutron radiation shielding polymer was therefore developed to minimize the effects of secondary radiation. Based on a literature search, the health effects in human tissue and organs were extensively studied for both actual radiation exposure and in radiation modeling.

Also, through a literature search, both active and passive radiation shielding systems were considered. Passive shielding systems based on current publications already exist and are used today for a variety of applications. Considering material and fabrication cost, weight, outgassing, and scalability, PVOH was determined to meet the requirements for spacecraft. Several published studies indicated that PVOH composites containing natural cellulose fibers were of interest due to their structural properties and low toxicity, therefore this study focused on the matrix polymer without the reinforcing fiber. Polyethylene, a well-known neutron moderator, was also fabricated and tested and compared to PVOH.

Modeling the shielding efficiency for both GCR and SPE radiation of MDPE and PVOH for spacecraft applications was accomplished using OLTARIS. The aluminum slab model initially was compared to an equal thickness (7.4 cm) of slabs consisting of polyethylene, PVOH, and PVOH cross-linked with borax. For both GCR and SPE radiation, the aluminum slab showed the greatest decrease in dose equivalent through the entire 7.4 cm thickness. However, a 7.4 cm thick aluminum slab with a 6 mm thick polymer backing layer resulted in a more abrupt decrease in GCR dose equivalent in the polymer layer. For SPE radiation, the initial decrease was less abrupt, then continued from 382 mSv/day to just over 335 mSv/day.

The polymer performance from OLTARIS was in contrast to the actual test results using a 1 Ci Americium-Beryllium neutron source, most likely due to the lack of protons, heavy ions, and electrons in the incident radiation and the different efficiencies for GCR and SPE radiation. For the experimental data, the dose equivalent percent reduction for polyethylene was plotted for 3 thicknesses: 2.1, 4.3, and 6.5 mm. Five samples of pristine PVOH and one cross-linked PVOH sample were also plotted. The dose equivalent for all but one pristine PVOH sample were less than that of polyethylene by about 0.9 mSv/day. A very similar radiation shielding performance was shown in polyethylene and PVOH, both in the OLTARIS models and the neutron testing results. Both PVOH and cross-linked PVOH would meet the requirements for a multifunctional composite matrix material suitable for spacecraft applications using cellulose fiber reinforcement.

REFERENCES

[1] “Moon to Mars,” *NASA*. [Online]. Available: https://www.nasa.gov/specials/moon2mars/. [Accessed: 05-Dec-2019].

[2] T.-H. Hou, J. Wilson, B. Jensen, S. Thibeault, C. Chang, and R. Kiefer, “E-beam Processing of Polymer Matrix Composites for Multifunctional Radiation Shielding,” *Space 2005*, 2005.

[3] J.W.Wilson, et al., "Issues in deep space radiation protection," *Acta Astronautica*, vol 49, Issues 3–10, pp 289-312, 2001.

[4] J.W. Wilson, F.A. Cucinotta, M.-H.Y. Kim, W. Schimmerling “Optimized Shielding for Space Radiation Protection,” *Physica Medica* , vol. XVII, Supplement 1, 2001.

[5] S. A. Thibeault, J. H. Kang, G. Sauti, C. Park, C. C. Fay, and G. C. King, “Nanomaterials for radiation shielding,” *MRS Bulletin*, vol. 40, no. 10, pp. 836–841, 2015.

[6] Oak Ridge Associated Universities, (NRC), “Radiation Safety Principles,” 2012, https://www.nrc.gov/docs/ML1122/ML11229A671.pdf [Accessed 3-Dec-2019].

[7] “Sunspots at Solar Maximum and Minimum,” NASA, [Online]. Available: https://earthobservatory.nasa.gov/images/37575/sunspots-at-solar-maximum-and-minimum/. [Accessed: 12-May-2020].

[8] R.A. English, R.E. Benson, V. Bailey, and C.M. Barnes, "Apollo Experience Report - Protection Against Radiation," NASA-TN D-7080, NASA, Washington, USA, 1973.

[9] J.L. Modisette, M.D. Lopez, and J.W. Snyder, "Radiation Plan for the Apollo Lunar Mission," *AIAA 7th Aerospace Sciences Meeting*, Paper No. 69-19, 1969.

[10] C. D. Camp & K. K. Tung, "Surface warming by the solar cycle as revealed by the composite mean difference projection," *Geophysical Research Letters*, vol 34, issue 14, 2009.

[11] Space Radiation” (ebook), NASA, [Online]. Available: https://www.nasa.gov/sites/default/files/atoms/files/space_radiation_ebook.pdf, [Accessed: 12/5/2019].

[12] NASA, “Understanding Space Radiation,” FS-2002-10-080-JSC (NASA Facts), 2002.

[13] P. Haskins, et al., “Contribution of Secondaries to the Space Radiation Environment on Space Missions,” Adv. Space Res. Vo|. 14, No. 10, pp. (10)943-(10)946, 1994.

[14] L. W. Townsend, A. M. Adamczyk, C. M. Werneth, H. M. Moussa, and J. P. Townsend, “Estimates of extreme solar particle event radiation exposures on Mars,” *Progress in Nuclear Science and Technology*, vol. 4, pp. 793–797, 2014.

[15] F. A. Cucinotta, S. Hu, N. A. Schwadron, K. Kozarev, L. W. Townsend, and M.-H. Y. Kim, “Space radiation risk limits and Earth-Moon-Mars environmental models,” *Space Weather*, vol. 8, no. 12, 2010.

[16] “RAD,” NASA, 08-Aug-2019. [Online]. Available: https://marsprogram.jpl.nasa.gov/msl/mission/instruments/rad/. [Accessed: 14-Jan-2019].

[17] J. Valentin, “The 2007 Recommendations of the International Commission on Radiological Protection,” ICRP Publication 103, 2007.

[18] NCRP,| Bethesda, MD. (2019).*NCRP, Bethesda, MD*. [online] Available at: https://ncrponline.org/ [Accessed 21 Nov. 2019].

[19] NASA (National Aeronautics and Space Administration), "NASA space flight human system standard, vol.1: crew health," NASA-STD-3001 (Approved 03-05-2007), NASA, Washington, USA, 2007.

[20] J. C. Chancellor, G. B. I. Scott, .and J. P. Sutton, “Space Radiation: The Number One Risk to Astronaut Health beyond Low Earth Orbit,” *Life* pp. 491-510, 2014.

[21] Carreau, Mark, “Kelly Exposes Challenges Of Human Deep Space Flight,” *Aerospace Daily & Defense Report*, March 9, 2016.

[22] J.C. Chancellor G.B.I. Scott, and J.P. Sutton, "Space Radiation: The Number One Risk to Astronaut Health beyond Low Earth Orbit," *Life*, 4, pp. 491-510, 2014.

[23] R.A.Norda and C.S. Wong, "Molecular targets in radiation-induced blood-brain barrier disruption," *Int. J. Radiation Oncology Biol. Phys.*, Vol. 62, No. 1, pp. 279 –287, 2005.

[24] V.K. Parihar, et al., "Cosmic radiation exposure and persistent cognitive dysfunction," *Nature Scientific Reports* 6, Article No. 34774, 2016. DOI: 10.1038/srep34774.

[25] M.M. Acharya, et al., “New Concerns for Neurocognitive Function during Deep Space Exposures to Chronic, Low Dose-Rate, Neutron Radiation,” *eNeuro* 6(4), 2019.

[26] F.A. Cucinotta, M. Alp, F.M. Sulzman, and M. Wang, "Space radiation risks to the central nervous system," *Life Sciences in Space Research* 2, 54-69, 2014.

[27] M.D. Delp, J.M. Charvat, C.L. Limoli, R.K. Globus, and P. Ghosh, "Apollo Lunar Astronauts Show Higher Cardiovascular Disease Mortality: Possible Deep Space Radiation Effects on the Vascular Endothelium," *Nature Sci. Reports* 6:29901, 2016, DOI: 10.1038/srep29901

[28] NBC News, "Deep Space Radiation Caused Heart Problems for Apollo Astronauts," 2016, [Online]. Available: https://www.nbcnews.com/health/heart-health/deep-space-radiation-caused-heart-problems-apollo-astronauts-n618116, [Accessed: 9-Aug-2016.

[29] V.A. Convertino, "Status of cardiovascular issues related to space flight: Implications for futureresearch directions," *Respiratory Physiology & Neurobiology* 169S, S34–S37, 2009.

[30] M. Boerma, G.A. Nelson, V. Sridharan, X-W. Mao, I. Koturbash, and M. Hauer-Jensen, "Space radiation and cardiovascular disease risk," *World J Cardiolv*.7(12), 882–888, 2015.

[31] C. Fuglesang, L. Narici, P.G. Picozza, W.G. Sannita, "Phosphenes in low earth orbit: survey responses from 59 astronauts," *Aviat Space Environ Med*, 77 (4), 449-52, 2006.

[32] W.G. Sannita, L. Narici, P. Picozza, "Positive visual phenomena in space: A scientific case and a safety issue in space travel," *Vision Research* 46, 2159–2165, 2006.

[33] T.F. Budinger, H. Bichsel, and C.A. Tobias, "Visual Phenomena Noted by Human Subjects on Exposure to Neutrons of Energies Less than 25 Million Electron Volts," Science 172 (3985), 868-870, 1971.

[34] S. Beatriz Zanello, C.A. Theriot, C. Prospero-Ponce, P. Chevez-Barrios, "Spaceflight Effects and Molecular Responses in the Mouse Eye: Observations After Shuttle Mission STS-133," Gravitational and Space Res., vol. 1, pp. 29-46, 2013.

[35] X.W. Mao, et al., "Spaceflight environment induces mitochondrial oxidative damage in ocular tissue,". *Radiation Res.,* 180:340–350, 2013.

[36] "NASA SBIR & STTR Program Homepage," NASA, [Online]. Available: https://sbir.nasa.gov/, [Accessed: 3-Dec-2019.

[37] L. W. Townsend, "HZE particle shielding using confined magnetic fields," *Journal of Spacecraft and Rockets*, vol. 20, no. 6, pp. 629–630, 1983.

[38] R. P. Joshi, H. Qiu, and R. K. Tripathi, "Configuration studies for active electrostatic space radiation shielding," *Acta Astronautica*, vol. 88, pp. 138–145, 2013.

[39] R. H. Levy and G. S. Janes, "Plasma radiation shielding," *AIAA Journal*, vol. 2, no. 10, pp. 1835–1838, 1964.

[40] M. Feychting, “Health effects of static magnetic fields—a review of the epidemiological evidence,” *Progress in Biophysics and Molecular Biology*, vol. 87, no. 2-3, pp. 241–246, 2005.

[41] H. Nittby, et al., “Radiofrequency and Extremely Low-Frequency Electromagnetic Field Effects on the Blood-Brain Barrier,” *Electromagnetic Biology and Medicine*, vol. 27, no. 2, pp. 103–126, 2008.

[42] M. A. EI-Ahdal, "Polyvinyl Alcohol-Lead Nitrate Paint for Gamma Radiation Installations," *Arab J. Nuc. Sci. and Appl.*, v. 40(1); p. 157-166, 2007.

[43] S. M. Badawy, and A.A. Abd El-Latif, "Synthesis and characterizations of magnetite nanocomposite films for radiation shielding," *Polymer Composites*, 38(5):974–980, 2017.

[44] K. Srinivasan and E. J. J. Samuel, "Evaluation of Radiation Shielding Properties of the Polyvinyl Alcohol/Iron Oxide Polymer Composite*," J Med Phys.*, Oct-Dec; 42(4): 273–278, 2017.

[45] F. Kazemi, S. Malekie, and M. A. Hosseini, "A Monte Carlo Study on the Shielding Properties of a Novel Polyvinyl Alcohol (PVA)/WO3 Composite, Against Gamma Rays, Using the MCNPX Code," *J Biomed Phys Eng.*, 9(4), 465–472, 2019.

[46] R. K. Fakher Alfahed, K. K. Mohammad, M. S. Majeed, H. A. Badran, K. M. Ali and B. Y. Kadem, "Preparation, morphological, and mechanical characterization of titanium dioxide TiO2)/polyvinyl alcohol (PVA) composite for gamma-rays radiation shielding," *J. of Phys: First International Scientific Conference Al-Ayen University*, 30–31 March, 2019.

[47] V. Thongpool, A. Phunpueok, N. Barnthip., and S. Jaiyen, "BaSO4/Polyvinyl Alcohol Composites for Radiation Shielding," *Applied Mech. and Mat.*, vol. 804, pp. 3-6, 2015.

[48] S. Nambiar, and J. T. W. Yeow, "Polymer-Composite Materials for Radiation Protection," *ACS Appl. Mater. Interfaces*, 4(11), 5717–5726, 2012.

[49] E. B. Iverson, “Spallation Neutron Source,” 2016, [Online], Available: https://conference.sns.gov/event/56/attachments/64/99/Lecture_2a_-_Neutron_Moderation_-_Erik_Iverson.pdf .[Accessed 3-Dec-2019].

[50] A. Munter, *Neutron Scattering Lengths and cross sections*, 30-Jan-2003. [Online]. Available: https://www.ncnr.nist.gov/resources/n-lengths/list.html. [Accessed: 21-Nov-2019].

[51] V. F. Sears, “Neutron scattering lengths and cross sections,” *Neutron News*, vol. 3, no. 3, pp. 26–37, 1992.

[52] J.A. Shusterman, et al., "The surprisingly large neutron capture crosssection of ^{88}Zr," *Nature* 565, 328–330, 2019.

[53] S. Nambiar and J.T. W. Yeow, "Polymer-Composite Materials for Radiation Protection," *ACS Appl. Mater*. Interfaces 4, 5717−5726, 2012. dx.doi.org/10.1021/am300783d.

[54] National Aeronautics and Space Administration (2005). *Revolutionary Concepts of Radiation Shielding for Human Exploration of Space,"* NASA-STD-3001, 2005.

[55] R.C. Singleterry, Jr., and S.A. Thibeault, "Materials for Low-Energy Neutron Radiation Shielding," NASA/TP-2000-210281, June 2000.

[56] S. C. Ko, C. S. Pugh, R. L. Kiefer, R. A. Orwoll, S. A. Thibeault, and G. C. King, "Boron Containing Polyimides for Aerospace Radiation Shielding," *MRS Proceedings*, vol. 551, 1998.

[57] V. F. Sears, "Neutron scattering lengths and cross sections," *Neutron News*, vol. 3, no. 3, pp. 26–37, 1992.

[58] J. S. Joy, "Mixed Lithium-Boron Materials," *Advances in Science and Technology*, vol. 45, pp. 1941–1943, 2006.

[59] T. Hayashi, K. Tobita, Y. Nakamori, and S. Orimo, "Advanced neutron shielding material using zirconium borohydride and zirconium hydride," *Journal of Nuclear Materials*, vol. 386-388, pp. 119–121, 2009.

[60] K. Okuno, "Neutron shielding material based on colemanite and epoxy resin," *Rad. Protect. Dosimetry*, Vol. 115, Issue 1-4, pp. 258-261, 2005.

[61] K. Ninyong, E. Wimolmala, N. Sombatsompop, K. Saenboonruang "Potential use of NR and wood/NR composites as thermal neutron shielding materials," *Polymer Testing* 59, 336-343, 2017.

[62] A. M. Sukegawa, Y. Anayama, K. Okuno, S. Sakurai, and A. Kaminaga, "Flexible heat resistant neutron shielding resin," *Journal of Nuclear Materials*, vol. 417, no. 1-3, pp. 850–853, 2011.

[63] M. Celli, F. Grazzi, and M. Zoppi, "A new ceramic material for shielding pulsed neutron scattering instruments," *Nuclear Instruments and Methods in Physics Research Section A: Accelerators, Spectrometers, Detectors and Associated Equipment*, vol. 565, no. 2, pp. 861–863, 2006.

[64] S. Chen, M. Bourham, and A. Rabiei, “Applications of Open-cell and Closed-cell Metal Foams for Radiation Shielding,” *Procedia Materials Science*, vol. 4, pp. 293–298, 2014.

[65] A. Morioka, et al., “Development of 300°C heat resistant boron-loaded resin for neutron shielding,” *Journal of Nuclear Materials*, vol. 367-370, pp. 1085–1089, 2007.

[66] J.E. Estevez, M. Ghazizadeh, J.G. Ryan, A.D. Kelkar, "Simulation of Hydrogenated Boron Nitride Nanotube’s Mechanical Properties for Radiation Shielding Applications," *Int. J. Chem., Nucl. Mat. and Met. Eng.* Vol:8, No:1, 2014.

[67] E.W. Taylor, "Organics, polymers and nanotechnology for radiation hardening and shielding applications," *Proc. of SPIE* Vol. 6713 671307-1, 2007. doi: 10.1117/12.729156

[68] C. Harrison, S. Weaver, C. Bertelsen, E. Burgett N. Hertel, E. Grulke, "Polyethylene/Boron Nitride Composites for Space Radiation Shielding," *J. Appl. Polymer Sci*., Vol. 109, 2529–2538, 2008.

[69] K. Okuno, “Neutron shielding material based on colemanite and epoxy resin,” *Radiation Protection Dosimetry*, vol. 115, no. 1-4, pp. 258–261, 2005.

[70] “3M 10B Enriched Boron.” [Online]. Available: http://multimedia.3m.com/mws/media/958420O/3m-10b-enriched-boron.pdf. [Accessed: 18-Nov-2019].

[71] American Elements, “Boron-10 Carbide Isotope,” *American Elements*, 13-Jun-2017. [Online]. Available: https://www.americanelements.com/boron-10-carbide-isotope-200443-95-4. [Accessed: 18-Nov-2019]

[72] Cambridge Isotope Laboratories, “Boron-10 Metal (10B, 92-99%),” *Cambridge Isotope Laboratories - BLM-1546-PK*. [Online]. Available: https://shop.isotope.com/productdetails.aspx?itemno=BLM-1546-PK. [Accessed: 18-Nov-2019].

[73] Sigma-Aldrich, “Boric acid-10B 426156,” *Sigma*. [Online]. Available: https://www.sigmaaldrich.com/catalog/product/aldrich/426156. [Accessed: 27-Nov-2019].

[74] M. Saltmarsh, *Essential guide to food additives*. Cambridge: Royal Society of Chemistry, 2013. ISBN 9781849735605

[75] M. M. Rahman, S. Afrin, and P. Haque, “Characterization of crystalline cellulose of jute reinforced poly (vinyl alcohol) (PVA) biocomposite film for potential biomedical applications,” *Progress in Biomaterials*, vol. 3, no. 1, Mar. 2014.

[76] H. Awada, D. Montplaisir, and C. Daneault, “The Development of a Composite Based on Cellulose Fibres and Polyvinyl Alcohol in the Presence of Boric Acid,” *BioResources*, vol. 9, no. 2, 2014.

[77] F. Guo, et al., “Low-Cost Coir Fiber Composite with Integrated Strength and Toughness,” *ACS Sustainable Chemistry & Engineering*, vol. 4, no. 10, pp. 5450–5455, 2016.

[78] N. A. Azahari, N. Othman, and H. Ismail, “Biodegradation Studies of Polyvinyl Alcohol/Corn Starch Blend Films in Solid and Solution Media,” *J. Phys. Therapy Sci.*, 22(2), pp. 15-31, 2010.

[79] N. Mallick, D. Pal, and A. B. Soni, “Corn-starch/polyvinyl alcohol bio-composite film for food packaging application,”*AIP Conf. Proc.*, 2201, 020005, 2019.

[80] N. Othman, N. A. Azahari, and H. Ismail,” Thermal Properties of Polyvinyl Alcohol (PVOH)/Corn Starch Blend Film,” *Malaysian Polymer Journal*, Vol. 6, No. 6, p 147-154, 2011.

[81] “OLTARIS Home Page,” *NASA*. [Online]. Available: https://oltaris.larc.nasa.gov/. [Accessed: 05-Mar-2019]

[82] R.C. Singleterry, et al., "OLTARIS: On-Line Tool for the Assessment of Radiation in Space," NASA/TP–2010-216722, July, 2010.

[83] NCRP 153, National Council on Radiation Protection and Measurements. "Information Needed to Make Radiation Protection Recommendations for Space Missions Beyond Low-Earth Orbit" (2006)

[84] T. C. Slaba, S. R. Blattnig, GCR environmental models II: Uncertainty propagation methods for GCR environments, Space Weather, 12, 225–232, 2014.

[85] "Radiation Uncertainties for Constellation Missions," NASA. [Online]. Available: https://oltaris.nasa.gov/help_documentation/uncertainties.html, [Accessed: 20-May-2020].

[86] G. D. Badhwar and P. M. O'Neill, "Long-term modulation of galactic cosmic radiation and its model for space exploration," *Advances in Space Research*, vol. 14, no. 10, pp. 749-757, 1994.

[87] G. Badhwar and P. O'Neill, “Galactic cosmic radiation model and its applications," *Advances in Space Research*, vol. 17, no. 2, pp. 7-17, 1996.

[88] P. M. O'Neill, “Badhwar-O'Neill galactic cosmic ray model update based on advanced composition explorer (ACE) energy spectra from 1997 to present," *Advances in Space Research*, vol. 37, no. 9, pp. 1727-1733, 2006.

[89] S. Golge, “NASA galactic cosmic radiation environment model: Badhwar-ONeill (2014), ”*Proceedings of The 34th International Cosmic Ray Conference - PoS(ICRC2015)*, 2016.

[90] “ACE,” *NASA*. [Online]. Available: https://science.nasa.gov/missions/ace/. [Accessed: 11-Nov-2019].

[91] P.M. O’Neill, S. Golge, T.C. Slaba, “Badhwar - O’Neill 2014 Galactic Cosmic Ray Flux Model Description,” NASA/TP-2015-218569, March, 2015.

[92] P. O'Neill, Badhwar-O'Neill, "2010 Galactic Cosmic Ray Flux Model; Revised," Nuclear Science, IEEE Transactions on, vol. 57, pp. 3148-3153, 2010.

[93] R. Rios, “NASA GCR Environment Model” [Online]. Available:https://indico.cern.ch/event/390724/contributions/1824639/attachments/1166840/1700326/nasa_gcr.pdf. [Accessed: 11-Nov-2019].

[94] T.C. Slaba, K. Whitman, “Badhwar - O’Neill 2020 Model,” NASA/TP-2019-220419, Nov, 2019.

[95] J.W. Wilson, L.W. Townsend, W. Schimmerling, G.S. Khandelwal, F. Khan, J.E. Nealy, F.A. Cucinotta, L.C. Simonsen, J.L. Shinn, J.W. Norbury, “Transport Methods and Interactions for Space Radiations,” NASA Reference Publication 1257, 1991.

[96] P. Jiggens, M. Chavy-Macdonald, G. Santin, A. Menicucci, H. Evans, A. Hilgers, "The magnitude and effects of extreme solar particle events," *J. Space Weather Space Clim.* vol. 4, 2014.

[97] F.A. Cucinotta, M-H.Y. Kim, L.J. Chappell, “Evaluating Shielding Approaches to Reduce Space” NASA/TP-2019-220419, May, 2012.

98 T.C. Slaba, S.R. Blattnig, J.W. Norbury, A.R., C.L. Tessa, and S.A. Walker, “GCR Simulator Reference Field and a Spectral Approach for Laboratory Simulation,” NASA/TP-2015-218698, March, 2015.

[99] “NIST Chemistry WebBook,” NIST Office of Data and Informatics. [Online]. Available: https://webbook.nist.gov/chemistry/index.html. [Accessed: 14-Mar-2019]

[100] “RRUFF Project website,” M. Scott and M. Origlieri, Accessed 7/31/2019, Internet: http://www.rruff.info

[101] C.E. Weir, "Infrared Spectra of the Hydrated Borates," *J of Research, National Bureau of Standards, Phys and Chem* vol. 70A, No.2, pp. 153-164, 1966.

[102] J.W. Marsh, D.J. Thomas, and M. Burke, “High resolution measurements of neutron energy spectra from Am-Be and Am-B neutron sources,” *J. Nuclear Instruments and Methods in Physics Research A* 340-348, 1995.

[103] R.H. Olsher and D.T. Seagraves, "Proton recoil scintillator neutron rem meter," Patent (Appl) US 6,529,573 B2, Mar. 4, 2003